

RELATIVISTIC ACCRETION DISK MODELS OF HIGH STATE BLACK HOLE X-RAY BINARY SPECTRA

SHANE W. DAVIS¹, OMER M. BLAES¹, IVAN HUBENY², AND NEAL J. TURNER³

Draft version September 11, 2018

ABSTRACT

We present calculations of non-LTE, relativistic accretion disk models applicable to the high/soft state of black hole X-ray binaries. We include the effects of thermal Comptonization and bound-free and free-free opacities of all abundant ion species. Taking into account the relativistic propagation of photons from the local disk surface to an observer at infinity, we present spectra calculated for a variety of accretion rates, black hole spin parameters, disk inclinations, and stress prescriptions. We also consider nonzero inner torques on the disk, and explore different vertical dissipation profiles, including some which are motivated by recent radiation MHD simulations of magnetorotational turbulence. Bound-free metal opacity generally produces significantly less spectral hardening than previous models which only considered Compton scattering and free-free opacity. It also tends to keep the effective photosphere near the surface, resulting in spectra which are remarkably independent of the stress prescription and vertical dissipation profile, provided little dissipation occurs above the effective photosphere. This robustness is due to the fact that the disk scale height is largely independent of the stress and dissipation when the disk is radiation pressure supported and electron scattering dominated throughout its interior. Our model spectra may be affected by continuing theoretical uncertainties that we do not account for, and we discuss these uncertainties. We provide detailed comparisons between our models and the widely used multicolor disk model. Frequency dependent discrepancies exist that may affect the parameters of other spectral components when this simpler disk model is used to fit modern X-ray data. For a given source, our models predict that the luminosity in the high/soft state should approximately scale with the fourth power of the empirically inferred maximum temperature, but with a slight hardening at high luminosities. This is in good agreement with observations.

Subject headings: accretion, accretion disks — black hole physics — radiative transfer — X-rays:binaries

1. INTRODUCTION

The high state spectral energy distribution (SED) of black hole X-ray binaries is dominated by a soft thermal component generally believed to be emission from an optically thick accretion flow. It is often hypothesized that the geometry of this flow is a radiatively efficient, geometrically thin disk (Shakura & Sunyaev 1973, hereafter SS73) or at higher luminosities a less radiatively efficient slim disk (Abramowicz et al. 1998). Most sophisticated spectral modeling of black hole accretion disks has focused on the case of supermassive black holes. However, models that compute vertical structure and radiative transfer have been constructed for Galactic black hole candidates assuming thin disk (Shimura & Takahara 1995, hereafter ST95; Merloni, Fabian & Ross 2000) and slim disk (Wang et al. 1999) relations.

ST95 argue that a simple diluted blackbody provides adequate fits to the local specific flux F_ν for regions of the disk which produce most of the X-ray photons. They conclude this for disks with sufficiently high luminosity over a range of luminosities, black hole mass, and black hole spin. The local specific flux is then given by

$$F_\nu = \frac{\pi}{f_{\text{col}}^4} B_\nu(f_{\text{col}} T_{\text{eff}}) \quad (1)$$

where B_ν is the Planck function, T_{eff} is the effective temperature of the emitting surface, and f_{col} is the color correction. They find that in many cases most of the disk spectrum is well approximated by a multi-temperature diluted blackbody with a single value of f_{col} . Furthermore, the value of f_{col} is not a strong function of the disk parameters. They attribute these results to saturated Comptonization playing a dominant role and producing Wien-like spectral profiles. The relative constancy of f_{col} in these model annuli has been used to justify fitting high state SED's with the multicolor blackbody model (*diskbb* in XSPEC) of Mitsuda et al. (1984). Although this model assumes a simple profile of effective temperature with radius, $T_{\text{eff}} \propto R^{-3/4}$, and does not account for relativistic transfer effects, it has been used to infer inner radii and black hole spins for disks believed to extend deep within the gravitational potential of the black hole.

Merloni et al. (2000) caution against assuming a nearly constant value for f_{col} . They construct several constant density disk models with a range of accretion rates. They assume some fraction of the released gravitational energy dissipates directly into an optically thin corona above the disk (Svensson & Zdziarski 1994), but they do not account for the irradiation of the disk surface by the coronal emission. They fit the resulting SED's with the *diskbb* model, apply relativistic corrections to the best fit parameters, and use the results to infer an inner radius for the disk. They find that the value of f_{col} needed to obtain the correct radius varies significantly from model to

¹ Department of Physics, University of California, Santa Barbara, CA 93106

² Steward Observatory and Department of Astronomy, University of Arizona, Tucson, AZ 85721

³ Jet Propulsion Laboratory, MS 169-506, California Institute of Technology, Pasadena, CA 91109

model.

Gierliński & Done (2004; hereafter GD04) investigate temperature and luminosity evolution in a sample of black hole binaries observed in the high state with the *Rossi X-ray Timing Explorer (RXTE)*. They fit their X-ray spectra with a model that includes a *diskbb* component and accounts for Comptonized emission from a corona, focusing on observations in which the Comptonized emission is $< 15\%$ of the bolometric luminosity. They find that many of the well observed sources are consistent with weak evolution of f_{col} in which f_{col} increases with higher luminosity or temperature. Furthermore, they tentatively conclude that such evolution is inconsistent with a modified stress prescription in which the accretion stress scales with only the gas pressure and not the total pressure.

To our knowledge, all the detailed theoretical models of thermal disk spectra of black hole X-ray binaries have so far neglected the effects of bound-free opacity of metal ions. (This is in marked contrast to models of reflection spectra in these systems.) Bound free opacity can often dominate free-free opacity at observed X-ray energies, reducing the relative importance of electron scattering and therefore altering the expected color correction factors. This may therefore affect the fits to high/soft state spectra and their interpretation. Bound-free opacity also imparts absorption/emission edges in the spectrum which are potentially observable, particularly with the high throughput spectra being produced by modern X-ray observatories.

In addition, significant theoretical advances have been made recently in understanding the nature and vertical distribution of turbulent dissipation (Turner 2004), as well as highlighting the possibility of significant external torques on the disk at the innermost stable circular orbit (e.g. Gammie 1999; Krolik 1999; Hawley & Krolik 2002). These results imply substantial modifications of the basic assumptions underlying the disk models upon which all spectral calculations have been based thus far.

In this paper, we construct fully relativistic accretion disk model atmospheres and examine the integrated SED's from these disks. We fully account for bound-free opacity by incorporating non-LTE rate equations for the ground-state level populations of all abundant metal ions. We focus on understanding the sensitivity of these SED's to the underlying assumptions in our models. We compare our results with previous theoretical investigations and recent observations. In section 2 we review the method used to construct our models. We describe our standard models in detail in section 3. We report our results from altering the stress prescription in section 4, adding an inner torque in section 5, and modifying the dissipation profile in section 6. In section 7 we compare our model SED's with the work of GD04. We provide further discussion of all these results and a summary of our conclusions in sections 8 and 9. Readers primarily concerned with the observational implications of our models may wish to skip directly to sections 7, 8, and 9.

2. METHOD

We construct models using the methods described in a series of papers (Hubeny & Hubeny 1997, 1998, hereafter HH98; Hubeny et al. 2000, Hubeny et al. 2001, hereafter HBKA). We construct thin disk models by solving the

fully relativistic one zone disk structure equations in the Kerr metric (Novikov & Thorne 1973, hereafter NT73; Page & Thorne 1974; Riffert & Herold 1985). Next, we compute the vertical structure and local spectra for annuli evenly spaced in $\log r$ where $r = R/R_g$, R is the Boyer-Linquist radial coordinate, and $R_g = GM/c^2$ is the gravitational radius. We compute ten annuli per decade in radius and assume the disk extends from the radius of marginal stability $r_{\text{in}} = r_{\text{ms}}$ to $r_{\text{out}} \approx 1000$. Emission from radii larger than r_{out} is assumed to be blackbody and contributes little to the integrated flux at photon energies $\gtrsim 0.1$ keV.

At each annulus, we use the TLUSTY stellar atmospheres code (Hubeny & Lanz 1995) to simultaneously solve the equations for the vertical structure and angle dependent radiative transfer. At X-ray temperatures, metal opacities are important, and we incorporate fully non-LTE ground state level populations for all ions of H, He, C, N, O, Ne, Mg, Si, S, Ar, Ca, Fe and Ni assuming solar abundances. Bound-free opacity due to each ion is included but bound-bound transitions are neglected. We account for Comptonization with an angle-averaged, Kompaneets treatment of the electron scattering source function. Finally, we calculate the integrated disk spectrum seen by an observer at infinity by using a fully general-relativistic transfer function (Agol 1997).

We make several approximations which may be violated in nature. The disk models are time steady and azimuthally symmetric. All heat is transported vertically by radiative energy flux. There is no mass loss from the disk, so the accretion rate is independent of radius. All radiative flux is assumed to originate within the disk and its atmosphere; irradiation of the disk surface due to an external X-ray source is neglected. Irradiation of the disk surface by returning radiation (Cunningham 1976) is also ignored. The atmosphere calculations are all one-dimensional despite evidence that radiation pressure supported accretion disks have significant inhomogeneity (Turner et al. 2003, Turner 2004).

For our base model (hereafter the standard model) we make additional assumptions which we later relax. First, there is no torque on the inner edge of the disk. Second, the energy dissipation rate per unit volume $\epsilon = \nabla \cdot \mathbf{F}$ is locally proportional to the density ρ . Third, we relate the vertically averaged stress, $\bar{\tau}_{r\phi}$, to the vertically averaged total pressure, \bar{P} using the prescription (SS73)

$$\bar{\tau}_{r\phi} = \alpha \bar{P}. \quad (2)$$

This standard model is parameterized by only four quantities: black hole mass M , spin parameter a , the stress parameter α , and accretion rate (SS73; NT73). The accretion rate is often expressed relative to the Eddington accretion rate as $\dot{m} = \dot{M}c^2/L_{\text{Edd}}$ where $L_{\text{Edd}} = 1.5 \times 10^{38} (M/M_{\odot}) \text{ erg s}^{-1}$ is the Eddington luminosity for completely ionized H. We prefer to use the quantity $l \equiv L/L_{\text{Edd}} = \eta \dot{m}$ as it relates more directly to the observed luminosity. Here L is the bolometric luminosity of the disk and $\eta(M, a)$ is the fraction of the energy at infinity which is radiated before crossing r_{ms} . The mass is fixed at $10M_{\odot}$ for all models considered here.

The atmospheres of the individual annuli are entirely determined by specifying the midplane column mass, the radiative flux, the local gravity, the composition and the vertical dissipation profile $\epsilon(z)$. The midplane column

mass m_0 is equal to half the surface density of the disk. The flux is parameterized by the effective temperature, T_{eff} , of the corresponding blackbody emitter. The vertical component of the gravitational acceleration $g = Qz$ is proportional to the distance z above the midplane and the constant of proportionality, Q , is a function only of R . These quantities (m_0 , T_{eff} , Q) are uniquely determined at a radius r in a one-zone model by a given set of disk parameters (M , l , α , a). As noted above, we consider $\epsilon(z) \propto \rho(z)$ for the standard models, but explore other prescriptions in section 6.

Except for the method of calculating m_0 , the standard models are equivalent to the supermassive black hole models described in HBKA and the reader is referred there for further details. HBKA solved a one-zone, algebraic relation for m_0 in terms of M , a , α , l , and r . This m_0 is then used throughout the stellar atmospheres calculation. Due to the simplifying assumptions of the one-zone model, there is no guarantee that equation 2 will hold for the converged solution. The vertically integrated pressure \bar{P} can be calculated from the converged non-LTE model so the consistency of this prescription can be checked after the fact using equation 2. The one-zone calculation provides a surprisingly accurate approximation, but order unity discrepancies do typically arise between the final α calculated from the converged non-LTE model and the input α .

We alter this prescription by using the initial m_0 to construct the LTE-grey model (Hubeny 1990) from which we calculate an α' with equation 2. If α' is within 10% of α we continue the full atmosphere calculation using the initial m_0 . Otherwise, we iterate by choosing a new m_0 , recomputing the LTE-grey model and α' until this condition is satisfied. We use Newton-Raphson to calculate the change in m_0 for the next iteration: $\delta m_0 = dm/d\alpha(\alpha - \alpha')$ with the derivative evaluated analytically assuming the one zone scaling holds. The resulting LTE-grey model is then used as the starting point for constructing the full non-LTE atmosphere. For most annuli, this method rapidly converges and provides a final α consistent (within $\sim 10\%$) with the input value. However, in some of the hottest annuli of the torqued disk model, the method fails to converge due to inaccuracies in the LTE-grey model. In this case, we default to the one-zone calculation for *all annuli* in the disk, but in all other cases we utilize the iterative procedure.

3. THE STANDARD MODEL

3.1. The Local Spectrum

The disks in X-ray binaries with a black hole accretor can be much hotter than a disk in a cataclysmic variable or quasar. The gas temperatures at the surface of these disks are sufficiently high ($\sim 10^6\text{K} - 10^7\text{K}$) that electron scattering dominates the opacity at typical photon energies and the emitted spectrum may deviate significantly from that of a blackbody (SS73).

We define the effective optical depth as

$$\tau_{\nu}^{\text{eff}} \equiv \int_0^m [3\kappa_{\nu}^{\text{th}}(\kappa_{\nu}^{\text{es}} + \kappa_{\nu}^{\text{th}})]^{1/2} dm' \quad (3)$$

where $\kappa_{\nu}^{\text{th}} = \kappa_{\nu}^{\text{ff}} + \kappa_{\nu}^{\text{bf}}$ is sum of the total bound-free and free-free absorption opacity, κ_{ν}^{es} is the electron scattering opacity, and m is column mass measured from the

surface. A closely related quantity is the depth of formation

$$\tau_{\nu}^* = \int_0^{m_{\nu}^*} (\kappa_{\nu}^{\text{es}} + \kappa_{\nu}^{\text{th}}) dm' \quad (4)$$

where m_{ν}^* is the *frequency dependent* column mass at which $\tau_{\nu}^{\text{eff}} = 1$. All of the disk models considered in this paper are effectively thick (i.e. $m_{\nu}^* < m_0$) at each annulus for frequencies of interest. In an electron scattering dominated atmosphere $\kappa_{\nu}^{\text{th}} \ll \kappa_{\nu}^{\text{es}}$ for typical photon energies implying that the photon destruction probability, $\epsilon_{\nu} = \kappa_{\nu}^{\text{th}}/(\kappa_{\nu}^{\text{th}} + \kappa_{\nu}^{\text{es}}) \ll 1$ and $\tau_{\nu}^* \gg 1$. Due to the temperature gradients in the atmosphere, the temperature at the depth of formation T_{ν}^* is generally greater than T_{eff} . In the absence of Comptonization, the frequency dependence of ϵ_{ν} and T_{ν}^* alter the spectrum and produce a modified blackbody.

Due to the potentially large number of scatterings ($n_{\text{es}} \approx \tau_{\nu}^{*2} \gg 1$), Comptonization may also be important. To account for its effect on our model spectra we *always* solve the radiative transfer equation including the Compton scattering source term. However, we still wish to have an indicator of the impact of electron scattering on the SED. For a homogeneous electron distribution, the y -parameter provides a simple means of characterizing the importance of Compton scattering. To gain similar insight, we generalize this prescription by defining a frequency dependent y -parameter (HBKA)

$$y_{\nu}^* \equiv \frac{4k_{\text{B}}T_{\nu}^*}{m_e c^2} \max[\tau_{\nu}^{*2}, \tau_{\nu}^*] \quad (5)$$

where k_{B} is Boltzman's constant, T_{ν}^* is the temperature at the depth of formation, m_e is the electron rest mass, and c is the speed of light.

In Figure 1, we plot the locally emitted SED from a single annulus with the frequency dependent quantities defined above. The model atmosphere was calculated for an annulus at $r = 12.6$ in a disk with $l = 0.1$ and $\alpha = 0.1$ accreting onto a Schwarzschild black hole. This is near where the flux (and thus the effective temperature) of the disk peaks. In the top panel (a) we compare the intensity at an inclination i of 55° to the vertical with that emitted by a diluted blackbody at the same T_{eff} with $f_{\text{col}} = 1.56$. The SED is a modified blackbody with a spectral break at the He-like Fe photoionization edge near 8.8 keV. Below this edge and above ~ 2 keV, the spectrum is well approximated by the diluted blackbody. In (b) we plot the relative contributions of electron scattering, free-free absorption, and bound-free absorption to the total opacity. The opacities are evaluated at m_{ν}^* . As expected, electron scattering dominates except at low energies and just blueward of the He-like Fe edge. Bound-free exceeds free-free absorption above ~ 1 keV and therefore should not be neglected. Note that a decrease in our frequency grid resolution below ~ 6 keV contributes to the breadth of the photoionization edges in that range. Panel (c) shows how τ_{ν}^* depends strongly on the presence of metals. As photon energy increases, the bound-free opacity overtakes the free-free opacity, preventing the depth of formation from exceeding 10. If we had neglected metal opacities, the depth of formation would continue to grow as the ratio of free-free to scattering opacity declined.

In that case, the photons reaching an observer are created deeper in the atmosphere where the temperatures and densities are higher. A direct consequence is seen in (d) where $y_\nu^* < 1$ for all frequencies of interest. Compton scattering may contribute to the broadening of photoionization edges, but it is *not* significantly altering the continuum. If we had neglected metals, the depth of formation would have been larger, the number of scatterings would have been higher, y_ν^* would have been greater than unity for $h\nu \gtrsim 2$ keV, and Comptonization would have had a larger effect.

Despite the limited role of Comptonization, the specific intensity is still reasonably well approximated by the diluted blackbody spectrum. A modified blackbody caused by dominant electron scattering opacity, strong temperature gradients, or both is generally not well characterized by a single temperature so this result is somewhat surprising. It seems to be due to the relative constancy of τ_ν^* over the range of photon energies near the peak. This means that most of the photons are being created by gas at a narrow range of temperatures and that the photon destruction probability is only weakly dependent on frequency. Both of these effects lead to a more blackbody like spectral profile but T_ν^* is still larger than T_{eff} . In this case, $T_\nu^* \approx 1.5 - 1.6T_{\text{eff}}$ near the peak consistent with the $f_{\text{col}} = 1.56$ used for the plot. If we had neglected bound-free metal opacity and Comptonization, the absorption opacity would be more frequency dependent and the diluted blackbody would be a poorer match to the emission.

Electron scattering and temperature gradients also affect the angular dependence of the radiation field. As shown in Figure 2, the spectra are significantly limb darkened at frequencies above 0.1 keV and the degree of limb darkening is frequency dependent. The curves in Figure 2 show the normalized specific intensity for emission at $r = 12.6$ from an $l = 0.1$, $\alpha = 0.1$, and $a = 0$ disk model. The curves are normalized by the specific flux so that isotropic emission would have an ordinate of unity. (The reason we chose $i = 55^\circ$ in Figure 1 is that the limb darkened emission matches isotropic emission near this viewing angle.) The curves are plotted for photon energies of 0.21, 2.2., and 8.4 keV. In this case, the emission near the peak (2.2 keV) is well approximated by the results for a semi-infinite Thompson scattering atmosphere assuming a Rayleigh phase function (Chandrasekhar 1960). It is less limb darkened at lower frequencies and more limb darkened at higher frequencies due to the temperature gradient in the atmosphere.

3.2. Disk Integrated Spectra

We calculate four standard model disks with $\alpha = 0.1$ accreting onto a Schwarzschild black hole with $l=0.01, 0.03, 0.1, \text{ and } 0.3$. Although larger values of l are astrophysically interesting, we consider only models with $l \leq 0.3$. For $l \sim 1$, radial advection begins to become important and the assumption that all locally dissipated accretion power is radiated locally ceases to be accurate. In this regime, a slim disk model should be used in place of the thin disk model which is no longer self-consistent.

In Figure 3 we plot the standard model SED's (solid curves) observed from infinity at $i = 70^\circ$. At each value of l , we also plot best-fit, fully-relativistic spectra from Schwarzschild disks in which the local SED at each annu-

lus is assumed to be a diluted blackbody. These diluted blackbody disks have the same surface brightness and utilize the same transfer function as the standard model disks. Therefore, they do not directly match the *diskbb* model which assumes a simplified form for the radial dependence of the flux and neglects relativistic transfer effects. The best fit values of $f_{\text{col}} = 1.4, 1.46, 1.56, \text{ and } 1.62$ for the $l = 0.01, 0.03, 0.1, \text{ and } 0.3$ models respectively. Because of limb darkening, the fully non-LTE atmosphere spectra have a lower apparent luminosity than the isotropic diluted blackbodies at $i = 70$. To account for this, the diluted black body spectra are plotted at 81% of their intrinsic luminosity.

We performed the fits shown in Figure 3 by creating XSPEC table models from diluted blackbody spectra and the fully non-LTE spectrum at the same l and i . For each l and i , we use the non-LTE model SED to generate an artificial PHA data set using a diagonal response matrix with constant effective area. This data set is then fit over the 0.1-10 keV range with the corresponding diluted blackbody table model which has two parameters: f_{col} and the normalization. We account for the effects of limb darkening in the non-LTE atmospheres by fitting for the normalization of the diluted blackbody model and find that the best fit models deviate from the artificial spectra by less than 10-20% except out in the high energy tail. (In an observed source, this tail would have low photon statistics.) If we had not fit the normalization the deviations would be as large as 50% at higher inclinations.

Because a and M are fixed, the emitting area of the disk is fixed. An increase in luminosity can only result from an increase in the surface brightness of the disk surface. For blackbody emission, $\nu_{\text{peak}} \propto T_{\text{eff}}(r_{\text{max}}) \propto l^{1/4}$. The same general trend is observed for our models, but the scaling does not strictly hold due to deviations from isotropic blackbody emission in the atmosphere calculations. As l increases, it can be seen that standard model SED's become increasingly hard relative to a blackbody disk at the same luminosity. That is, the solid curves with high (low) l are better fit with diluted blackbodies with higher (lower) values of f_{col} . This relative hardening is largely due to the increased dominance of electron scattering in the more luminous models. The trend can be seen in Figure 4 where we plot the relative contributions of the opacity mechanisms at τ_ν^* in the $r = 12.6$ annuli. As l increases, the radiative flux increases and the metals become highly ionized. The corresponding decrease in the bound-free opacity at lower photon energies moves τ_ν^* nearer the midplane where the temperatures are larger. This produces a modified blackbody spectrum which is harder for higher values of l . For $l = 0.3$, only the highest ionization states of iron are sufficiently populated to provide significant bound-free opacity. This produces a larger value for τ_ν^* and $y_\nu^* \gtrsim 1$, implying that Comptonization is saturated.

ST95 attribute the effectiveness of the diluted blackbody approximation for their higher luminosity models to the presence of saturated Comptonization producing Wien-like spectra in the inner annuli of their disks. The impact of Compton scattering on our spectral calculations can be approximately estimated from Figure 5 in which we plot y_ν^* in the $r = 12.6$ annulus of each model.

We find that $y_\nu^* \gtrsim 1$ only in the $l = 0.3$ model (solid line). Nevertheless, the diluted blackbody spectra still deviate from the non-LTE model spectra by at most 10-20% at typical photon energies above 0.1 keV. As discussed in section 3.1, this is in part due to the relatively weak frequency dependences of T_ν^* and ϵ_ν near the spectral peak. The agreement between the two types of spectra generally improves with increasing l . The effects of increasingly saturated Comptonization may account for some of this trend. The reduction in bound-free opacity as the degree of ionization increases probably also plays a role since some of the deviations are associated with spectral breaks at the photoionization edges.

In constructing these SED's we have neglected the irradiation of the disk surface by an external corona. Provided the local ionization parameter of the irradiating coronal flux is sufficiently low, the reflection spectrum will be determined predominantly by the intrinsic ionization state of the disk. For illustration, we show the ionization fraction of iron at a Thompson depth of unity in Figure 6, for the $l = 0.3$ disk. Inside $r = 100$ Fe XXV is the dominant ion, with a small fraction of Fe XXVI and Fe XXVII at $r \gtrsim 10$. The drop in ionization state near $r \sim 6$ is due to the no-torque inner boundary condition. For this disk model, we expect the Fe K α line features in the reflection component to be dominated by the Fe XXV recombination line. Resonant trapping limits fluorescent line emission for Fe XVII through Fe XXIII (Ross & Fabian 1993) so any feature from more neutral iron must come from $r \gtrsim 1000$.

3.3. Dependence on Spin

In an X-ray binary, the case of non-zero black hole spin seems particularly plausible. Here we consider the ‘‘maximally spinning’’ $a = 0.998$ case (Thorne 1974) as an upper bound on the disk spin with the expectation that angular momentum extraction mechanisms likely limit real black holes to lower spin parameters.

Changing a modifies the one-zone radial disk structure equations and the location of r_{ms} (NT73). Near the event horizon, the relativistic effects on the photon geodesics are amplified, altering the SED observed from infinity. At fixed l , the accretion rate drops due to the increased efficiency. However, the innermost annuli are still hotter than in the Schwarzschild case and the SED is expected to be harder modulo relativistic effects on the geodesics.

We construct three maximally spinning Kerr models with $\alpha = 0.1$ accreting at $l = 0.01, 0.03,$ and 0.1 . Difficulties obtaining convergence in some of the inner annuli have so far prevented us from completing an $l = 0.3$ disk. In Figure 7, we plot the integrated SED's for these models observed at $i = 70^\circ$ by an observer at infinity. At each value of l , we also plot the best-fit, fully relativistic spectra from maximally spinning disks in which the spectrum at each annulus is assumed to be a diluted blackbody. We fit them with the method described in section 3.2. Comparison with Figure 3 shows that both the full atmosphere models and the diluted blackbody curves are harder than their Schwarzschild counterparts at the same l . Increasing a modifies the one-zone radial disk structure equations, yielding larger fluxes and correspondingly higher T_{eff} in the innermost annuli.

Relativistic broadening also accounts for the hardening of the SED. As a increases from zero to 0.998, r_{ms}

decreases from 6.0 to 1.23. Moving closer to the event horizon amplifies the relativistic effects on the photon geodesics, altering the SED observed from infinity. At $i = 70^\circ$, strongly blue-shifted emission from matter moving toward the observer pushes the high energy tail to larger frequencies. In Figure 8, we plot the same set of models as viewed from a lower inclination of $i = 45^\circ$. The relativistic broadening is clearly reduced and both the spectral peak and the high energy tail occur at lower energies.

In the hot inner annuli, the metals are highly ionized. Even for iron, a substantial fraction of the atoms are completely stripped of electrons in the $l = 0.1$ model. This reduces the bound-free opacity and electron scattering plays a more dominant role than in the Schwarzschild case. As a result, the diluted blackbody models which best approximate the solid curves generally have higher values of f_{col} and the breaks near the metal edges are not as prominent. A calculation for these hotter annuli finds $y_\nu^* \gtrsim 1$ for most relevant photon energies in the $l = 0.03$ and 0.1 models. The agreement between the diluted blackbody and atmosphere model SED's improves with increasing l . For $i = 70^\circ$, the maximum deviations are always less than or equal to those in the corresponding Schwarzschild model. Since bound-free opacity is reduced, the ratio of absorption to scattering is much more frequency dependent for the higher luminosity models and the improved agreement between the two types of spectra is likely due to Comptonization. The local limb darkening at characteristic photon energies emitted by the hot inner annuli is even better approximated by that of a semi-infinite Thompson scattering atmosphere (Chandrasekhar 1960) than the Schwarzschild case depicted in Figure 2.

3.4. Dependence on α

As discussed in section 2, the set of three parameters $m_0, T_{\text{eff}},$ and Q along with the abundances and dissipation profile, uniquely determine the structure and spectrum of an annulus in our models. Of these quantities, only m_0 depends on α . If all other quantities are fixed, an increase (decrease) in α produces a larger (smaller) stress. For the accretion rate to remain constant, there must be a corresponding reduction (increase) in the surface density and therefore in m_0 . In a constant density, radiation pressure dominated one-zone model, a change in m_0 leads to an equivalent fractional change in the density because the scale height is independent of α (SS73).

In Figure 9 we compare the vertical temperature and electron number density n_e profiles in disks with different values of α . The solid and dashed curves correspond to $\alpha = 0.1$ and 0.01 respectively. We plot results for annuli at $r = 12.6$ in disks with $a = 0$ and $l = 0.1$. Both of these atmospheres are expected to be radiation pressure dominated so we scale the z coordinate with the appropriate one-zone model h (HH98 eq. 53). The x's in Figure 9 mark the location of τ_ν^* evaluated at a frequency near the spectral peak ($\nu_{\text{peak}} \approx 5 \times 10^{17} \text{ Hz}^{-1}$).

Below one scale height the models are consistent with the predictions of a one-zone model. The densities are nearly constant and n_e in the $\alpha = 0.01$ atmosphere is about a factor of ten larger than in the $\alpha = 0.1$ case. The flux rises linearly with z providing a force that balances gravity. However, above $z = h$ the flux rises less steeply

and begins to asymptote to σT_{eff}^4 . Gas pressure gradients are therefore needed to balance the continued increase in gravity and the density decreases exponentially. The x 's indicate that most of the spectrum is formed where the density is dropping rapidly and not where the density is relatively constant. Disk models which neglect vertical gradients in density will therefore overestimate the ratio of absorption to scattering opacity and underestimate the effective Compton y -parameter.

Despite their differences for $z \lesssim h$, the temperature and density profiles seen from the surface down to τ_ν^* are nearly identical in the two annuli. In other annuli at larger r and smaller T_{eff} , the τ_ν^* surfaces move further from the midplane so that regions of spectral formation remain near the surface where the density decreases exponentially. In general, the temperature, density and ion level population profiles of the two models still do not differ significantly in these surface regions at any r . In Figure 10 we compare the integrated SED's from these disks viewed at $i = 70^\circ$. They are nearly indistinguishable.

4. THE STRESS PRESCRIPTION

Most of the standard model disks (α -disks) presented in section 3 are radiation pressure dominated in the innermost annuli. Such disks have long been known to be “viscously” and thermally unstable. One way to avoid these instabilities is to construct models (hereafter β -disks) in which the accretion stress scales with gas pressure P_{gas} rather than total pressure P in equation (2) (Lightman & Eardley 1974). It has been argued that such a scaling could be the consequence of magnetic field buoyancy limiting magnetic stresses (Sakimoto & Coroniti 1981; Stella & Rosner 1984).

As discussed in section 3.4, altering the stress prescription only changes m_0 in a one-zone model. A process that limits the magnetic stress (e.g. magnetic field buoyancy) may also alter the vertical dissipation profile, but we discuss the impact of the dissipation profile separately in section 6. For fixed α , replacing P by P_{gas} in equation (4) results in a lower stress. Thus, a β -disk requires a larger m_0 to produce the same accretion rate as an α -disk. The larger m_0 results in greater midplane densities and temperatures.

We construct β -disk models with $\alpha = 0.1$ for Schwarzschild black holes with $l = 0.03, 0.1$, and 0.3 and maximally spinning Kerr black holes with $l = 0.03$ and 0.1 . At $l = 0.01$ the α -disk models are gas pressure dominated down to r_{in} and are therefore equivalent to β -disks. We calculate m_0 by integrating the LTE-grey model until equation (2) is satisfied for $P = P_{\text{gas}}$. In Figure 11, we compare the integrated SED's of the Schwarzschild models with the equivalent α -disk spectra for an observer at $i = 70^\circ$. The results for the maximally spinning Kerr models are similar. We find that the stress prescription has little effect on the black hole disk SED's for the same reasons as in section 3.4. Specifically, τ_ν^* lies near the surface of the disk where the vertical structure of the two types of annuli are always similar regardless of the conditions at the midplane. Photons emitted at τ_ν^* in the β -disks encounter nearly identical profiles of density, temperature, and level populations as those in an α -disk.

5. TORQUES ON THE INNER BOUNDARY

The no-torque boundary condition may be invalid if magnetic fields keep the material in the plunging region causally connected to the disk (Gammie 1999; Krolik 1999). In that case, the surface density and brightness of the disk are modified from the standard model. The corresponding changes in $T_{\text{eff}}(r)$ and $m_0(r)$ can be parametrized in terms of $\Delta\eta$, the change in efficiency of converting energy into radiative flux (Agol & Krolik 1998). For a Schwarzschild black hole with no inner torque, $\eta = 0.057$. We calculate a torqued Schwarzschild disk with $l = 0.1$, $\alpha = 0.1$, and $\Delta\eta = 0.05$ so that the efficiency is nearly double the no-torque case. Since we fix the luminosity of the two disks, the accretion rate of the torqued disk is lower. Our method of integrating the LTE-grey model fails to converge for some of the hottest annuli so we use the one-zone calculation to find m_0 throughout the disk. We computed the values of α required to satisfy equation 2 in the converged non-LTE annuli, and they differed from the assumed value by less than 50 percent. For the reasons discussed in section 3.4, we do not expect the resulting spectrum to be sensitive to this small discrepancy. In the disk without a torque, T_{eff} increases with decreasing r until reaching a maximum at $r_{\text{max}} > r_{\text{ms}}$ and then falls to zero at r_{ms} . For the torqued disk, $r_{\text{max}} = r_{\text{ms}}$ and T_{eff} continues to rise all the way down to the inner edge of the disk. Despite the decrease in \dot{m} , the fluxes in the innermost annuli are higher than in a standard disk at the same luminosity.

In Figure 12, we compare the SED's of the torqued (solid) and standard model (dotted) disks viewed at $i = 70^\circ$. Using the same surface brightness and folding through the same transfer function, we also calculate spectra assuming the local emission produces an isotropic diluted blackbody with a best-fit $f_{\text{col}} = 1.61$. Owing to the larger fluxes, the innermost annuli of the torqued disk are hotter and the SED is much harder. In these annuli, the metals are highly ionized and provide little opacity. Comptonization is saturated leading to annuli with Wien-like spectral profiles. The diluted blackbody is still good to about 10% for frequencies at or below the peak. The torqued disk requires a slightly larger f_{col} than the corresponding standard model disk.

One motivation for examining torqued disks is the hope that they might be well approximated by a *diskbb* model. Since the *diskbb* model is relatively inexpensive to calculate it is particularly useful for fitting data. It assumes a simple surface brightness profile which ignores the no-torque inner boundary condition and the relativistic corrections to the disk structure equations. The surface brightness of the torqued disk provides a better match to this profile so we fit our fully relativistic models with the *diskbb* model. Fits for the disk models with no inner torque are discussed in section 7.

We perform the fits by first generating XSPEC table models from our model SED. Next, we use these table models along with the *XMM-Newton* European Photon Imaging Camera pn (EPIC-pn) response matrices to create artificial PHA data sets. We also account for the intervening Galactic absorption with a neutral absorber model. Accounting for photoelectric absorption is important because it affects the statistical weight of the bins used in the fits. The absorption reduces the relative

fraction of photon counts on the low energy end of the EPIC-pn band and makes the fit more sensitive to the emission at higher energies. We choose a H column of $5 \times 10^{21} \text{cm}^{-2}$ as a representative value for a typical X-ray binary source. We also assume the source is at 5 kpc with 75 ksec exposure, providing a high signal-to-noise ratio dataset. We then fit these data with a *diskbb* model over the 0.3-10 keV energy range including the same absorption used to generate the artificial spectrum. The reduced χ^2 of the fit is poor with $\sim 20\%$ deviations below 1 keV and $\sim 10\%$ differences near the spectral peak. The best-fit *diskbb* model is narrower than our model, providing a deficit of flux at the high and low energy ends of the band and an excess near the spectral peak. This is in part due to the departures from blackbody emission, but is due mostly to relativistic transfer effects and the remaining differences in the surface brightness profile. Considering a larger torque would increase the similarity in the surface brightness profiles. This should improve the quality of the fit but discrepancies would remain. Even when we assume locally isotropic blackbody emission with a surface brightness identical to the *diskbb* model, the resulting SED is intrinsically broader than the *diskbb* due to the effects of relativistic transfer.

6. THE DISSIPATION PROFILE

In section 2 we stated that our standard model assumes that the energy dissipation rate per unit volume ϵ is locally proportional to the density ρ . Before exploring other dissipation profiles, it is worthwhile reminding the reader what this implies for a radiation pressure dominated disk. In that case, hydrostatic balance reduces to

$$\frac{-1}{\rho} \frac{dP_{\text{rad}}}{dz} = \frac{\kappa_F F}{c} = \frac{GM}{R^3} \frac{C}{B} z \quad (6)$$

where $P_{\text{rad}} \sim P$ is the radiation pressure, C and B are general relativistic correction factors (Riffert & Herold 1985), and κ_F is flux mean opacity. In these scattering dominated disks, $\kappa_F \approx \kappa^{\text{es}}$ which is only weakly dependent on z through the free electron fraction. Therefore $F \propto z$, implying that ϵ is constant when the gradient in radiation pressure balances gravity. Our assumption that $\epsilon \propto \rho$ then implies that the density is constant so long as gas pressure gradients are negligible. From the definition of column mass $dm = -\rho dz$, it is easy to see that our assumption reduces to

$$\epsilon = \rho \left(-\frac{dF}{dm} \right) = \rho \frac{\sigma T_{\text{eff}}^4}{m_0} \quad (7)$$

where σ is the Stefan-Boltzman constant. The first equality holds by definition and the second follows from our assumption which implies dF/dm is independent of m . We have set $F(m) = \sigma T_{\text{eff}}^4 (1 - m/m_0)$ in all the models discussed above.

6.1. Physically Motivated Dissipation Profiles

We would like to examine how the choice of $F(m)$ affects the vertical structure of the accretion disk but there is no firm theoretical basis to guide our analysis. It is commonly accepted that the magnetorotational instability (MRI, Balbus & Hawley 1991) can provide a means for tapping the free energy of the differential rotation

and producing turbulence in which energy may cascade irreversibly from large to small scales. However, the nature of non-radiative vertical energy transport and the mechanisms for dissipation in these disks are still not well understood. Despite these uncertainties, there is a rather robust prediction of magnetic field buoyancy in radiation dominated annuli (Sakimoto & Coroniti 1981; Stella & Rosner 1984). It is therefore quite reasonable to expect that a larger fraction of the dissipation occurs nearer the surface than is assumed in equation 7.

Numerical simulations which include radiative diffusion in a vertically stratified disk (Turner 2004) bear out this prediction. The radiation-MHD equations are solved for a patch of disk centered at $200 R_g$ from a $10^8 M_\odot$ black hole. Magnetic field energy is produced fastest by the MRI two to three density scale heights away from the midplane. The magnetic field is buoyant and rises toward the surface at approximately the Alfvén speed. The density is more centrally concentrated than in a standard model disk with the same surface density and radiative flux. The time averaged dissipation is not at all consistent with the $\epsilon \propto \rho$ assumption as much of the dissipation takes place in the low density surface layers.

Similar calculations are not yet available for disks accreting onto $10M_\odot$ black holes. In order to explore the possible consequences of magnetic buoyancy, we choose a form for dF/dm which approximates the Turner (2004) results for a $10^8 M_\odot$ black hole. We then use this form to calculate $F(m)$ with choices of m_0 and T_{eff} appropriate for an annulus around a $10M_\odot$. Although these simulations are the best quantitative model for $F(m)$ available, this choice should not be considered overly restrictive. There is still considerable uncertainty in the simulation itself. Although 29% of the dissipation is due to Silk damping (Agol & Krolik 1998), most is still the result of numerical reconnection. Furthermore, the outermost grid zone is quite optically thick but our models extend to $\tau \ll 1$ so there are several decades in m for which $F(m)$ is not constrained by the simulation results. Following HH98, we approximate dF/dm as a broken power law with m being the dependent variable. The broken power law is parametrized by a division point $m_d = f_d m_0$ and exponents above (ζ_1) and below (ζ_0) the division. For the standard model, $\zeta_0 = \zeta_1 = 0$. In the simulation, the dissipation and density are functions of position and time so we average the domain horizontally and we average over time from 20 to 40 orbits. The broken power law provides a reasonable approximation with $\zeta_0 = -0.9$, $\zeta_1 = 0$, and $f_d = 0.004$ so we do not consider more complicated profiles.

Next we insert this choice of dF/dm in an annulus with m_0 and T_{eff} appropriate for $r = 12.6$ in a $l = 0.1$, $a = 0$, $\alpha = 0.1$, and $10M_\odot$ standard model disk. We had difficulties obtaining convergence for non-LTE models in which the Eddington factors were updated after each solution of the radiative transfer equation. If we instead fix the Eddington factors after the first radiative transfer solution, the models converge. We believe the lack of convergence in the first case is a result of our calculation method rather than an instability in the model. Furthermore, we doubt the assumption in the second case has a strong effect on the resulting spectra. The maximum fractional change in the Eddington factors after a global solution of the radiative transfer is less than 3% for

all frequencies and depths and is generally significantly smaller.

The resulting annulus structure (dotted curve) is compared with the corresponding standard model (solid curve) in Figure 13. The two are quite different. The radiative flux is plotted in the top panel. For $z < h$, the solid curve rises linearly because the radiative flux must balance the linearly increasing vertical gravity. The dotted curve falls below this line so the gradient in the gas pressure also provides significant support against gravity in the modified annulus. The temperature is shown in the middle panel. The surface layers above $\tau = 1$ (marked by the squares) are somewhat hotter in the modified annulus owing to the increased fraction of dissipation in that model. The electron number density is shown in the bottom panel. The density is more centrally concentrated than in the standard model annulus as a density gradient is necessary to compensate for the reduced radiation pressure support. The temperatures and densities at τ_ν^* (marked by x's) are nearly equal in the two models, though the shape of the temperature and density profiles are more dissimilar from each other than in the models with differing stress prescriptions.

The specific intensities at $i = 55^\circ$ are plotted in Figure 14. The SED of the modified annulus is slightly harder giving an f_{col} which is about 10% higher and the He-like Fe absorption edge at 8.8 keV becomes an emission edge. Despite these differences, the model spectra are still qualitatively quite similar. The strong temperature inversion in the modified annulus is above the photosphere for frequencies redward of the 8.8 keV edge and has little effect on the resulting SED.

6.2. Dissipation and Coronae

The geometry and origin of the coronae in accretion disks remain uncertain. One plausible explanation is that the coronae are due to hot electrons heated by reconnection of magnetic fields in the optically thin layers at the disk surface. This is the essence of the Svensson & Zdziarski (1994) model where it is assumed that some fraction of released energy is transported without dissipation to a corona above the disk. It can be seen from the top panel of Figure 13 that very little dissipation occurs above the Thompson photosphere in the models described in 6.1. We have considered several different prescriptions for $F(m)$ in which larger fractions of the dissipation occur at low m . The choice of a broken power law for dF/dm provides a smooth, continuous dissipation profile which is different from the Svensson & Zdziarski (1994) model in which dF/dm would be a step function.

In Figure 15, we show two annuli in which almost half of the dissipation occurs above the Thompson photosphere. The first case (solid curve) is similar to a Svensson & Zdziarski (1994) model in that dF/dm is constant below the photosphere as in the standard model disks, but dF/dm is discontinuous at the photosphere. Nearly 50% of the dissipation occurs above a Thompson depth of unity and the resulting annulus has a sharp rise (drop) in the temperature (density) just above the scattering photosphere. In order to better approximate these gradients, we increase our number of depth points but memory restrictions then limit us to just considering H, He, C, N, O, and Fe for this annulus only. The neglect of less abundant

species seems to have little effect on the vertical structure or spectrum. In the second case (dotted curve) dF/dm is a continuous broken power law with $\zeta_0 = -1.1$, $\zeta_1 = 0$, and $f_d = 0.0001$. About 40% of the dissipation occurs above the Thompson photosphere and another $\approx 20\%$ occurs above τ_ν^* (measured near the peak). We consider the same m_0 and T_{eff} used for the models plotted in the Figures 13 and 14. The profiles in the discontinuous model closely resemble those of a standard model disk below the photosphere, but above there is a sharp rise in the temperature and drop in the density. In the second case, the shape of the density and temperature profiles are similar to the modified annulus discussed in section 6.1 but on a more exaggerated scale. The surface layers are much more extended, the surface temperature and central density are higher, and the densities at the surface are lower.

We plot the SED's of these annuli in Figure 16. In the top panel we plot the specific intensity at 55° . In both cases, Compton scattering by the hot thermal electrons above the photosphere produces a steep tail with emission up to ~ 100 keV. These tails are only crudely approximated by a power law as there is curvature at low energies near the peak and at high energies due to the thermal cutoffs. The discontinuous model (solid curve) produces a slightly harder spectrum. A flatter, more power law-like tail such as is commonly observed could presumably be produced by choosing a more top heavy $F(m)$, but the surface temperatures become too large and our treatment of Compton scattering is no longer valid. We also include power law curves with photon indices of $\Gamma = 3.4$ and 3.5 to approximate the two spectra over the $\sim 5 - 50$ keV band. In the bottom panel we plot the ratio of the model SED's to these power laws. For the discontinuous model there is curvature due to the reduction in the scattering albedo from bound-free opacity above ~ 10 keV and the spectrum resembles the putative Compton reflection hump. The high energy side of the hump is due to both Compton down scattering by the cooler electrons near the photosphere and the thermal cutoff of the hot electrons. There is a strong emission feature at the He-like Fe edge. This feature is likely enhanced because our treatment only allows recombinations to the ground state. Some fraction of this power would be shifted to lower energies if we had considered recombinations to excited levels. In the second case, the spectrum simply falls off at high energies and there is no structure in the residuals which could be characterized as a reflection hump. A large fraction of dissipation occurs in the spectral forming regions just below the photosphere so the temperature there is high and the density is relatively low. Almost all iron is completely ionized so that the bound-free opacity which produces the low energy side of the hump in the previous model is insignificant.

7. LUMINOSITY - TEMPERATURE RELATION

Detailed fits to individual observations are beyond the scope of this paper. Because we neglect irradiation of the disk surface, we focus on comparison with the results of GD04. Their sample is particularly relevant because they select observations in which the coronal emission is less than 15% of the bolometric luminosity of the source.

GD04 construct plots of the temperature-luminosity

relation for each source in their sample. The luminosity of the disk model L_{disk} is plotted as a fraction of L_{Edd} versus the maximum color temperature T_{max} . A major difficulty with inferring the physical properties of accretion disks is that the distance, inclination and black hole mass of the source are often not all known with great accuracy. Therefore, the vertical and horizontal position of the locus of points on these curves is uncertain. However, the shape of the locus of points for an individual source should be robust to such uncertainties.

If the disk spectrum is well approximated by a multitemperature diluted blackbody with fixed f_{col} , L_{disk} should be proportional to T_{max}^4 . Specifically, Gierliński et al. (1999) assume that the gravitational field may be approximated with a pseudo-Newtonian potential (Paczynski & Witta 1980) and find the relation

$$\frac{L_{\text{disk}}}{L_{\text{Edd}}} \approx 0.583 \left(\frac{1.8}{f_{\text{col}}} \right)^4 \left(\frac{M}{10M_{\odot}} \right) \left(\frac{kT_{\text{max}}}{1\text{keV}} \right)^4 \quad (8)$$

where $T_{\text{max}} = T_{\text{eff,max}} f_{\text{col}}$. GD04 find that most of the sources roughly follow this scaling, though several show some degree of relative hardening (increasing f_{col}) as L_{disk} increases.

One obstacle to comparing with their results is that neither T_{max} nor f_{col} is a well defined theoretical quantity in our models. In principle, we could use the f_{col} values from the best-fit models shown in Figure 3, but that fitting procedure is quite different from the method implemented by GD04. In constructing their temperature-luminosity diagram, they fit the *diskbb* model to their spectra to account for the presumed disk component. They then use the best fit inner temperature and total model flux to calculate $L_{\text{disk}}/L_{\text{Edd}}$ and T_{max} . In doing so they apply relativistic correction factors (Zhang, Cui & Chen 1997) for a Schwarzschild black hole at the appropriate inclination. They also apply an additional correction factor to account for the mismatch between the surface brightness profile of the *diskbb* model and the pseudo-Newtonian potential used to derive equation 8.

To facilitate comparison, we try to reproduce this procedure as closely as possible. We produce an artificial EPIC-pn PHA data set as described in section 5. We also generate a second set of artificial spectra by the same method but employing the *RXTE* Proportional Counter Array (PCA) response matrices. Galactic absorption has less impact on the PCA photon statistics so we do not include it in those artificial spectra and fits. The EPIC-pn spectra are useful because of the high signal-to-noise and the low energy coverage while the PCA spectra are necessary for comparing with GD04. Next, we fit *diskbb* models over the 0.3-10 keV and 3-20 keV energy ranges for the EPIC-pn and PCA data sets respectively. We also generate artificial spectra including a *compTT* (Titarchuk 1994) component which is 10% of the bolometric flux to account for possible Comptonized coronal emission. These spectra are then fit with a combined *diskbb* + *compTT* model. We find that the best fit parameters of the *diskbb* models are only weakly sensitive to the presence or absence of the *compTT* component as long as we fit for this component with another *compTT* model and *not* a power law. Finally, we apply the same prescription outlined in GD04 to calculate $L_{\text{disk}}/L_{\text{Edd}}$ and T_{max} from the model temperature and flux.

We show the results of this procedure for the four Schwarzschild models with $l = 0.01, 0.03, 0.1,$ and 0.3 viewed at $i = 45^\circ$ and 70° in Figure 17. The solid curves represent the luminosity-temperature relation of equation 8 for $f_{\text{col}} = 1.4, 1.6, 1.8$ and 2.0 . The triangles and squares mark the *XMM-Newton* EPIC-pn and the *RXTE* PCA measurements respectively. Only the highest three luminosities are plotted for the PCA measurements because the model with $l = 0.01$ emits only a small fraction of its luminosity above 3 keV and is not well constrained by a PCA observation. The *diskbb* model provides a poor fit to the artificial *XMM* data so reliable uncertainties cannot be estimated for best fit parameters. The uncertainties (90% confidence for one parameter) on PCA depend on the signal-to-noise of the simulated data set, but they are of order the symbol size or smaller for a 1.5 ksec exposure of a source at 5 kpc. We compare the best-fit *diskbb* spectra to the $i = 70^\circ$ non-LTE model SED's in Figure 18.

First, we focus on the EPIC-pn data sets. The filled and open triangles mark the $i = 45^\circ$ and 70° measurements respectively. Both sets of measurements show a similar degree of spectral hardening with increasing luminosity but with approximately the same fractional offset in T_{max} and $L_{\text{disk}}/L_{\text{Edd}}$ for each l . The difference in apparent luminosity between the two sets of measurements and the known l values are predominantly due to limb darkening in the atmospheres (compare with Figure 2), but there is also a small mismatch between our relativistic transfer function and the g correction factors we interpolate from Zhang et al. (1997) Table 1. Comparing the symbols with the solid lines shows that the derived values of f_{col} are inclination dependent. When folded through the spectral response, the best-fit *diskbb* models disagree with artificial spectra by about 5-10% at lower energy and less than 5% near the peak. These deviations can be significant for the high signal-to-noise obtained in a long exposure of the bright high/soft state X-ray binaries. The model provides poor fits (reduced $\chi^2 \gg 1$) to the data for the simulated 75 ksec exposures of sources at 5 kpc.

The PCA measurements at $l = 0.1$ and 0.3 agree reasonably well with the EPIC-pn data sets. The T_{max} values are larger because the PCA band only extends down to 3 keV in our fits and does not include the spectral peak. The Doppler-broadened high energy tail is consistent with a slightly higher inner temperature than the emission near the spectral peak which is given more weight in the fits to the EPIC-pn artificial spectra. The $l = 0.03$ case is slightly more complicated because there is a spectral break above 3 keV due the presence of bound-free opacity. This produces a slightly steeper fall-off in the high energy tail. This can be more easily fit by a lower temperature and correspondingly higher normalization leading to a larger $L_{\text{disk}}/L_{\text{Edd}}$ and lower T_{max} . These shifts overestimate the emission near the peak which is outside of the PCA band but must be accounted for in the EPIC-pn fits.

8. DISCUSSION

8.1. Comparison with Previous Work

Our models are qualitatively different from those of ST95 in several important ways. We examine the specific intensities and account for relativistic effects on photon

geodesics while they compare the specific flux in the local frame of the disk. Calculating specific fluxes in the local frame simplifies the comparison with diluted blackbodies by avoiding inclination-dependent effects. However, this has the drawback of neglecting the non-trivial coupling between frequency and inclination caused by the limb darkening and relativistic transfer which is presumably present in real accretion disks. Another important difference between our models is our inclusion of metals. We account for the bound-free opacity of all important ions in addition to free-free opacity which was the only absorption opacity included in their calculations. The addition of metal opacity reduces the range of l in which saturated Comptonization is important and produces modified blackbodies which are slightly softer (more consistent with lower values of f_{col}) than their model SED's.

ST95 conclude that multi-temperature, diluted blackbody spectra adequately approximate their models at higher luminosities but are inadequate at low luminosity. When they compare diluted blackbodies with their $\alpha = 0.1$, Schwarzschild black hole integrated disk spectra at energies above 0.1 keV, the deviations are less than 20%, 15%, and 30% for the $l = 0.0057, 0.057, \text{ and } 0.57$ models respectively. For the two more luminous models, the largest disagreement is at the low energy end of the band and the agreement is better at higher energies. For $l = 0.0057$, the integrated spectra show larger deviations at higher energies and the individual model annuli are not well represented by diluted black bodies because the y -parameter is small. They conclude that color-corrected blackbodies are good approximations only at the higher luminosities.

We focus on the integrated emission from the whole disk. For all the $l = 0.01$ to 0.3 models, the comparisons between diluted blackbody and non-LTE atmosphere model SED's depend on the viewing angle. In section 3.2, we presented fits to our non-LTE models with fully relativistic diluted blackbody models with constant color correction f_{col} . Provided one fits for both f_{col} and the normalization (in order to account for limb darkening), these fits are surprisingly good. The disagreement between the models is less than 20% at most photon energies regardless of inclination. As seen in Figure 3, the deviations in the high energy tails can eventually become much larger. However, by that point the statistical weight of these energy bins is typically low because the integrated photon flux falls off rapidly in the tail. The fitted values of f_{col} at $i = 70^\circ$ are summarized in the second column of Table 1. These best-fit values are weakly dependent on inclination, but they are always lower than the 1.7-1.9 values reported by ST95.

A direct comparison of our models with those of Merloni et al. (2000) is complicated by their assumption that a fraction f of the dissipation occurs in the corona. Inspection of their Figure 2 suggests that the value of f_{col} inferred from their spectral models is mostly determined by the corrected disk luminosity parameterized by $(1-f)\dot{m}$. Specifically, models with different f but the same $(1-f)\dot{m}$ yield similar values for f_{col} . Their \dot{m} accounts for the disk efficiency so this disk luminosity parameter is the rough equivalent of our l . Merloni et al. (2000) also construct artificial spectra from their model SED's using an *RXTE* response matrix. They fit these spectra with *diskbb* models and derive values of f_{col} by

a method which is similar, but differs in detail from the procedure implemented by us in section 7 and in GD04. They find a trend toward increasing f_{col} with decreasing $(1-f)\dot{m}$. If we take the *diskbb* fits of section 7 and use their method for determining f_{col} , we find the values listed in the fourth column of Table 1. (For completeness, we also show values appropriate for the *XMM-Newton* EPIC-pn camera in the third column.) We find a weak increase in f_{col} with increasing l which is inconsistent with their results. We suspect that this discrepancy is largely due to their neglect of bound-free metal opacity which causes them to overestimate the ratio of scattering to absorption opacity. Therefore ϵ_ν is lower and τ_ν^* is greater, providing a higher T_ν^* . The higher T_ν^* and lower ϵ_ν would both give rise to harder, more modified spectra, consistent with larger values of f_{col} . These effects are most significant in the low accretion rate models where Comptonization is negligible at most radii. Their assumption of constant density likely overestimates the density in the spectral forming regions in both gas pressured and radiation pressure dominated annuli, increasing the ratio of absorption to scattering opacity at τ_ν^* . This reduces the y -parameter but may somewhat mitigate the increased spectral hardening which comes from neglecting metal opacity.

8.2. Stress Prescription and Dissipation Profile

For the range of l , α , and a explored here, altering m_0 by varying α or changing the stress prescription has little effect on the SED. Even changes in the vertical dissipation profile do not matter very much unless a substantial fraction of the heating occurs above the effective photosphere. It therefore appears that the spectra are insensitive to the details of the very uncertain vertical structure of disks, which might be encouraging from a theoretical point of view, but disappointing if one wants to use spectral observations to probe disk physics.

However, it is important to bear in mind how this robustness arises. The innermost parts of luminous black hole accretion disks are both radiation pressure supported and electron scattering dominated. Provided heat is vertically transported by radiative diffusion, then the scale height h , which determines the surface gravity g , is completely independent of the stress prescription. If there is little dissipation in the surface layers, the radiative flux is constant, but the gravity still increases with height. As a result, gradients in gas pressure are always important in maintaining hydrostatic equilibrium near the surface, and this always produces a very steeply declining density profile there. This is in contrast to the temperature profile, which is relatively constant in the surface layers (cf. Fig. 9), and close to the effective temperature. The steep decline in density occurs over a gas pressure scale height $H_g \sim P_{\text{gas}}/(\rho g)$ (Hubeny 1990), which is independent of the details of the overall vertical structure as it only depends on the surface temperature and the local gravity. The effective photosphere at characteristic frequencies is determined by

$$\tau^{\text{eff}} = \int [3\kappa^{\text{th}}(\kappa^{\text{es}} + \kappa^{\text{th}})]^{1/2} \rho dz = 1. \quad (9)$$

Because $\kappa^{\text{th}} \propto \rho$ and $\kappa^{\text{es}} \propto \rho^0$, this integral is approximately proportional to $\rho^{*3/2} H_g$. Hence the density ρ^*

at the effective photosphere is approximately independent of the details of the vertical structure. The column mass down to the effective photosphere $m^* \simeq \rho^* H_g$ and the temperature at the effective photosphere $T^* \simeq T_{\text{eff}}(\kappa^{\text{es}} m^*)^{1/4}$ will also be approximately independent of the vertical structure. The resulting spectrum will therefore be quite robust. This all fails, however, if heat is transported by other means, such as convection, rather than radiative diffusion. It may also fail if substantial density inhomogeneities are present within the disk turbulence, as we discuss below.

The robustness of the SED's to changes in the stress is also a feature of accretion disk models around supermassive black holes, and for the same reason. Figure 17 of Hubeny et al. (2000) show that accretion disk models around a $5 \times 10^8 M_\odot$ Kerr hole are very insensitive to the value of α for Eddington ratios up to at least $l \simeq 0.1$. The only discrepancies occur above the He II edge. Similar differences occur in stellar mass black hole models near the iron K edge, but this lies in the high energy tail of the spectrum. For high black hole spins and higher Eddington ratios, the effective optical depth of the innermost annuli is reduced, and the effective photosphere at all frequencies moves deeper into the disk atmosphere. In such cases the spectrum will start to depend on the stress and stress prescription, with high values of α or an α -disk prescription producing harder spectra than low values of α or a β -disk prescription. The dependence on α is illustrated for $l = 0.3$ disks accreting onto supermassive Kerr holes in Figure 16 of HBKA. We therefore expect that high Eddington ratio disk models around stellar mass Kerr holes to be less robust to changes in the stress prescription as well, but we have not yet succeeded in constructing such models.

The weak dependence of the model SED's on the choice of stress prescription casts some doubt on GDO4's speculation that their luminosity-temperature relations are inconsistent with β -disk models. Their reasoning relies on the assumption that Comptonization is not important in β -disks due to the larger midplane densities inferred from a one zone model (Nannurelli & Stella 1989). However, the effective photospheres in our models always occur in the surface layers where the densities are much less than the midplane density. Therefore, Comptonization is equally important (or unimportant depending on l) for both α -disks and β -disks over the range of parameters we consider.

In an attempt to inject first principles physics that is not present in the standard model, we also considered modifications to the vertical dissipation profile. The standard model dissipation profile produces a disk which is hydrodynamically unstable to convection in the radiation pressure dominated regions (Bisnovatyi-Kogan & Blinnikov 1977, HBKA), though it is far from clear whether significant convective transport of heat would occur in the presence of MRI turbulence. Magnetic field buoyancy suggests that the dissipation may be more concentrated near the surface than in the standard model. An annulus with a modified dissipation profile motivated by simulations of accretion disk turbulence (Turner 2004) produces a vertical structure that is increasingly gas pressure supported in its interior, and hydrodynamically stable to convection.

Adopting this modified dissipation profile only produces slight changes to the resulting spectrum, however. The reason is that the considerations of the first paragraph of this section still apply. The surface density profile is still very steep, and the physical properties of the plasma at the effective photosphere are largely independent of the dissipation profile, provided most of that dissipation occurs deeper than the effective photosphere. The impact is not completely negligible as the modified annulus SED is slightly harder than in the standard model, though the inferred f_{col} only differs by $\sim 10\%$. However, if we consider more top heavy dissipation profiles in which a significant fraction of the dissipation occurs near or above the photosphere we can produce atmospheres with very different SED's even though the surface radiative flux, gravity, and surface density are the same. The "corona"-producing annuli discussed in section 6.2 are extreme examples. These calculations may allow for a self-consistent treatment of the hard and soft spectral components in models in which the coronal emission is provided by flaring regions above the disk though there are several caveats to our treatment which remain to be addressed. These include the assumptions that the temperatures of the ions and electrons are equivalent, the electrons are entirely thermal, and the corona is time-steady.

Most of the uncertainties in the vertical distribution and nature of the dissipation are relatively easy to address with the methods presented here. However, other potentially important aspects of the dynamic nature of these disks remain unaccounted for in our models. Simulations (e.g. Turner 2004) suggest the presence of substantial inhomogeneities in density due to the compressible nature of the turbulence (Turner, Stone & Sano 2003) and radiatively driven instabilities (Gammie 1998). Modeling of the emergent spectrum from such structures requires three dimensional radiative transfer. We have reported on Monte Carlo radiative transfer calculations on inhomogeneous structures created by simulations elsewhere (Davis et al. 2003). The temperature regime was more appropriate for a quasar disk rather than an X-ray binary, and thermal Comptonization was negligible. The main effect of the inhomogeneities was to reduce the modified blackbody effects and produce a softer, more thermal spectrum. The emergent flux through an inhomogeneous medium is also larger than the spatially averaged flux required to support the medium against gravity (Begelman 2001). This may reduce the vertical scale height of the disk compared to the standard model, and make the emergent spectrum more sensitive to the stress prescription and dissipation profile. Because the turbulence is compressible and supersonic, bulk Comptonization can also significantly affect the emergent spectrum (Socrates, Davis & Blaes 2004). In addition to the effects of Silk damping, bulk Comptonization may also provide a radiative dissipation mechanism for the turbulence itself. It is also possible that the time-averaged spectrum emerging from a time-dependent, turbulent annulus differs from the spectrum emerging from a time-average of the vertical structure.

8.3. Observational Implications

Our luminosity-temperature relation agrees reasonably well with the results of GD04. For example, between

$l = 0.3$ and 0.1 we find weak evolution toward lower f_{col} consistent with that observed in XTE J1550-564. The larger decrease in f_{col} in our models from $l = 0.1$ to 0.03 is not clearly observed in their data, but it is not inconsistent due to large uncertainties in the fits at lower luminosities. The magnitudes of f_{col} derived using the procedure of GD04 depend on the inclination due to limb darkening. In this case, they are in approximate agreement with the observed values for $i = 70$, which is near the measured inclination of $73.5_{-2.7}^{+1.9}$ for XTE J1550-564 (Orosz et al. 2002). The values of f_{col} are probably also sensitive to our assumptions about inner torques, dissipation profiles, and metal abundances. Despite these concerns, we expect the generally weak trend toward decreasing f_{col} with decreasing l to be robust because it is largely due to the increasing ratio of absorption to scattering opacity as the temperature of the disk drops. This reduces ϵ_{ν} and moves τ_{ν}^* closer to the photosphere, lowering T_{ν}^* . The spectra soften and the associated f_{col} values decrease.

Though we employ the concept of a color correction throughout this paper for the purposes of comparison, we caution that isotropic, diluted blackbodies are *not* perfect approximations to our models. Given the high signal-to-noise spectra afforded by an observation with *XMM-Newton*, the $\lesssim 20\%$ discrepancies between the best fit, fully relativistic diluted blackbodies and the non-LTE atmosphere spectra are potentially significant. Any assumption of isotropy is clearly poor as limb darkening can alter the inferred luminosity of a source by up to 50% at high inclinations. We further caution that the *diskbb* model is an even poorer match to our model SED's. For high signal-to-noise observations we do not expect it to provide adequate fits unless the disk is truncated at large radius. Even if the presence of an inner torque makes the surface brightness profile more consistent with the *diskbb* profile, the model completely neglects relativistic transfer effects. The best-fit *diskbb* spectra are always significantly narrower than our models due to differences in the surface brightness profiles and relativistic broadening. To accurately model all the emission from a disk component, one needs to include the relativistic effects on the disk structure and transfer function in the spectral model *before* fitting it to the observed SED. The data in Table 1 indicate that different but seemingly consistent methods of calculating f_{col} with *diskbb* model fits give differing results. Furthermore, the results depend on the detector response and band.

These concerns are particularly relevant for higher signal-to-noise observations which have inferred relativistically broadened Fe K α lines but fit the disk component with an unbroadened *diskbb* model (Miller et al. 2004a, 2004b). In some cases the iron line profiles are so broad and asymmetric that they require a near maximally spinning black hole with a very steep iron line radial emissivity profile. Contrary to our expectations of 10-15% discrepancies, the *diskbb* model seems to account surprisingly well for the presumed disk component in these observations. We suspect this may be due in part to their use of a power law to model the coronal emission. If the disk provides the seed photons for the corona, a power law will likely overestimate the flux of this component at the low energy end of the band where

we predict the discrepancies are largest. This extra emission could account for the difference between our model SED's and the *diskbb* models. We test this hypothesis by constructing an artificial spectrum with our $l = 0.1$, $a = 0.998$, and $i = 45^\circ$ model SED, assuming it is located at 5 kpc and accounting for an intervening H column of $5 \times 10^{21} \text{ cm}^{-2}$. We also include a *compTT* component whose flux is about 10% of the model flux. First, we fit these data with a model that includes a *diskbb* component, a *compTT* component with the seed temperature fixed at the input value, and neutral absorption at the input H column. We get a poor fit with residuals of $\sim 15\%$. When we replace the *compTT* model with a power law, the residuals of the best fit are reduced to less than 5% and the quality of fit improves dramatically. It therefore seems plausible that the combinations of a *diskbb* and power law may effectively reproduce the SED of a real disk even though the *diskbb* model does not properly account for the accretion disk emission.

9. CONCLUSIONS

We have calculated several representative non-LTE, fully relativistic models for geometrically thin disks accreting onto a $10M_{\odot}$ black hole. We first explored the behavior of standard model (SS73, NT73) accretion disks. We found that the inclusion of abundant metals has a significant impact on the model SED's because of bound-free absorption opacity at high photon energies. The inclusion of this additional opacity generally decreases the importance of Comptonization, but still produces softer, more Wien-like spectra than would be expected from free-free opacity alone. The associated diluted blackbody color corrections are generally lower than found by previous authors (ST95, Merloni et al. 2000).

The frequency dependence of the disk integrated model SED's is qualitatively similar to that of spectra produced by assuming isotropic diluted blackbodies with constant color correction for the local emission, provided these local spectra are folded through a relativistic transfer function. Quantitative differences still exist which should be discernible for some observations with modern X-ray observatories. The effects of limb darkening are significant and the assumption of isotropy of the local emission must be compensated by fitting the normalization as well as the color correction. The best-fit f_{col} 's are weakly dependent on the black hole spin and accretion rate, generally increasing as either parameter increases.

We have found that the standard model SED's are strongly affected by changes in accretion rate and black hole spin, but they are only weakly dependent on the value of α for the parameter space explored here. Modifying the stress prescription by replacing P with P_{gas} in equation 2 also has little effect on the model SED's, contrary to the supposition of GD04. The reason for this is that the overall disk scale height in the inner, radiation pressure supported regions is largely independent of the stress prescription, and so are the resulting physical conditions at the effective photosphere. Higher Eddington ratio models, particularly those around maximally spinning holes, may be more sensitive to the treatment of the stress. Steep density gradients generally exist in the surface layers, and modeling the disk annuli with constant density slabs is also a poor approximation.

We found that our model SED's are generally not well

matched by a simple *diskbb* model over the whole 0.3-10 keV band. Fits using the *XMM-Newton* EPIC-pn response have discrepancies of greater than 10%. Such large discrepancies are generally not seen in *diskbb* fits to high signal-to-noise observations of X-ray binaries with relativistically broadened Fe K α lines. We speculate that the lack of residuals in these fits may be due to overestimation of the coronal emission at low energies. A resolution of this issue will require detailed fits of our models to real observations.

We used the method of GD04 to construct a luminosity-temperature relation for our Schwarzschild disk models. The luminosity scales as the fourth power of the temperature, but we also found a trend toward larger f_{col} with increasing l which is generally consistent with their analysis for several sources. The agreement with their measured values of f_{col} is somewhat more uncertain and our f_{col} measurements depend on the inclination due to limb darkening effects. The values of f_{col} which we infer using GD04's method are higher than those we derive from fits with the relativistic diluted blackbody models (see Table 1).

We have also looked at modifications of the standard model based on recent theoretical progress in understanding magnetohydrodynamic stresses in the flow.

Adopting a vertical dissipation profile derived from numerical simulations produces a large change in the vertical disk structure but has a weaker effect on the SED, consistent with a $\sim 10\%$ increase in the best-fit f_{col} . Profiles which have a greater fraction of the dissipation near the surface can produce much larger changes. Thus, our choice of dissipation profiles represents a large uncertainty in the models.

The addition of an inner torque at fixed fraction of the Eddington luminosity produces a significant hardening of the spectrum similar to that made by increasing the black hole spin. Unless the two types of models are distinguished by fits with detailed continuum models or relativistic line profiles, it may be difficult to infer either parameter without making an assumption about the other. Additional uncertainties in the disk physics that we have not explored here are the possibility of bulk vertical transport of heat, e.g. convection, and the effects of density inhomogeneities and bulk Comptonization in the supersonic disk turbulence.

We thank Phil Chang, Chris Done, and Aristotle Socrates for very useful discussions and suggestions. This work was supported by NASA grant NAG5-13228.

REFERENCES

- Abramowicz, M. A., Czerny, B., Lasota, J. P., & Szuszkiewicz, E. 1988, *ApJ*, 332, 646
- Agol, E. 1997, Ph.D. thesis, Univ. California, Santa Barbara
- Agol, E., & Krolik, J. 1998, *ApJ*, 507, 304
- Agol, E., & Krolik, J. H. 2000, *ApJ*, 528, 161
- Balbus, S. A. & Hawley, J. F. 1991, *ApJ*, 376, 214
- Begelman, M. C. 2001, *ApJ*, 551, 897
- Bisnovatyi-Kogan, G. S., & Blinnikov, S. I. 1977, *A&A*, 59, 111
- Chandrasekhar, S. 1960, *Radiative Transfer* (New York: Dover)
- Cunningham, C. T. 1975, *ApJ*, 202, 788
- Cunningham, C. T. 1976, *ApJ*, 208, 534
- Davis, S. W., Blaes, O. M., Tuner, N. J., & Socrates, A. 2004, in *ASP Conf. Ser. 311, AGN Physics with the Sloan Digital Sky Survey*, ed. G. T. Richards & P. B. Hall (San Francisco: ASP), 135
- Gammie, C. F. 1998, *MNRAS*, 297, 929
- Gammie, C. F. 1999, *ApJ*, 522, L57
- Gierliński, M., & Done, C. 2004, *MNRAS*, 347, 885 (GD04)
- Gierliński, M., Zdziarski, A. A., Poutanen, J., Coppi, P.S., Ebisawa, K., & Johnson W.N. 1999, *MNRAS*, 309, 496
- Hawley, J. F., & Krolik, J. H. 2002, *ApJ*, 566, 164
- Hubeny, I. 1990, *ApJ*, 351, 632
- Hubeny, I., Agol, E., Blaes, O., & Krolik, J.H. 2000 *ApJ*, 533, 710
- Hubeny, I., Blaes, O., Krolik, J.H., & Agol, E. 2001 *ApJ*, 559, 680 (HBKA)
- Hubeny, I., & Hubeny, V. 1997 *ApJ*, 484, L37
- Hubeny, I., & Hubeny, V. 1998 *ApJ*, 505, 558 (HH98)
- Hubeny, I., & Lanz, T. 1995, *ApJ*, 439, 875
- Krolik, J. H. 1999, *ApJ*, 515, L73
- Lightman, P., & Eardley, D. M. 1974, *ApJ*, 187, L1
- Merloni, A., Fabian, A.C. & Ross, R.R. 2000, *MNRAS*, 313, 193
- Miller, J. M., et al. 2004a, *ApJ*, 601, 450
- Miller, J. M., et al. 2004b, *ApJ*, 606, L131
- Mitsuda, K., et al. 1984, *PASJ*, 36, 741
- Nannurelli, M., & Stella, L. 1989, *A&A*, 226, 343
- Novikov, I.D. & Thorne, K.S. 1973, in *Black Holes*, eds. C. De Witt and B. De Witt (New York: Gordon & Breach) p. 343 (NT73)
- Orosz J. A. et al. 2002, *ApJ*, 568, 845
- Paczyński B., & Witta P. J. 1980, *A&A*, 88, 23
- Page, D.N., & Thorne, K.S. 1974, *ApJ*, 191, 499
- Riffert, H. & Herold, H. 1995, *ApJ*, 450, 508
- Ross, R. R. & Fabian, A. C. 1993, *MNRAS*, 261, 74
- Sakimoto, P.J., & Coroniti, F.V. 1981, *ApJ*, 247, 19
- Shakura, N. I., & Sunyaev, R. A. 1973, *A&A*, 24, 337 (SS73)
- Shimura, T., & Takahara, F. 1995, *ApJ*, 445, 780 (ST95)
- Socrates, A., Davis, S. W., & Blaes, O. 2004, *ApJ*, 601, 405
- Stella, L., & Rosner, R. 1984, *ApJ*, 277, 312
- Svensson, R., & Zdziarski, A. A. 1994, *ApJ*, 436, 599
- Thorne, K. S. 1974, *ApJ*, 191, 507
- Titarchuk, L. 1994, *ApJ*, 434, 570
- Turner, N. J. 2004, *ApJ*, 605, L45
- Turner, N. J., Stone, J. M., Krolik, J. H., & Sano, T. 2003, *ApJ*, 593, 992
- Wang, J. M., Szuszkiewicz, E., Lu, F. J., & Zhou, Y. Y. 1999, *ApJ*, 522, 839
- Zhang, S. N., Cui, W., & Chen, W. 1997, *ApJ*, 482, L155

TABLE 1
COLOR CORRECTIONS

l	f_{FR}	$f_{\text{MFR}}^{\text{X}}$	$f_{\text{MFR}}^{\text{R}}$	f_{GD}^{X}	f_{GD}^{R}
0.3	1.64	1.62	1.67	1.88	1.97
0.1	1.56	1.60	1.63	1.85	1.90
0.03	1.46	1.50	1.36	1.74	1.58
0.01	1.40	1.29	...	1.50	...

NOTE. — Calculations of f_{col} based on fits to our model spectra for $\alpha = 0.1$ disks around Schwarzschild black holes, viewed at an inclination of 70° . Each column uses a different method to determine f_{col} (see text). The second column summarizes f_{col} from our fits to the non-LTE model SED's with our fully relativistic diluted blackbody model spectra. A superscript X or R indicates the f_{col} values were calculated using the *diskbb* fits to the *XMM-Newton* EPIC-pn or *RXTE* PCA data sets respectively. A subscript MFR or GD04 means that we use the methods described in Merloni et al. (2000) or GD04 (respectively) to calculate f_{col} .

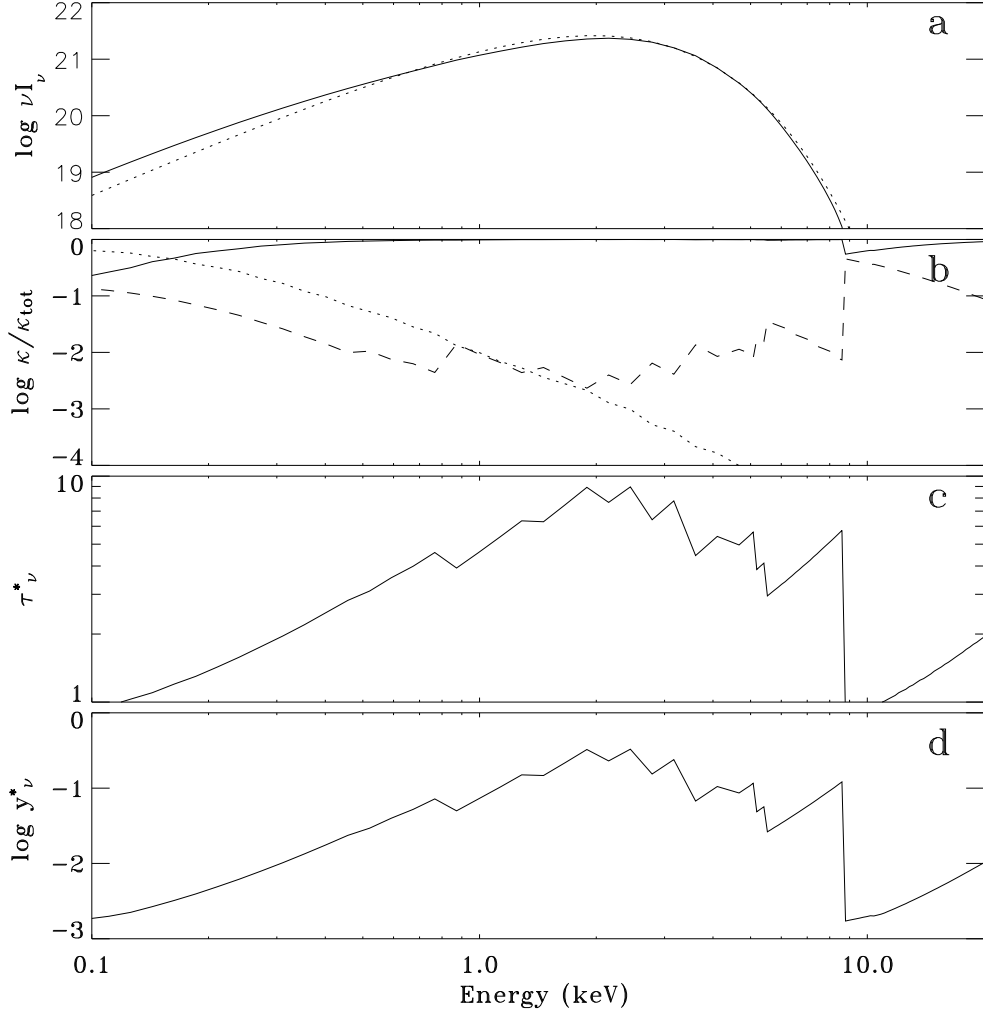


FIG. 1.— Specific intensity and other frequency dependent parameters evaluated in the local frame at $r = 12.6$ for a disk with $\alpha = 0.1$, $l = 0.1$, and $a = 0$. (a) We compare the specific intensity viewed from 55° (solid curve) with a diluted blackbody at the same T_{eff} and $f_{\text{col}} = 1.56$ (dotted curve). The units of the ordinate are $\text{ergs s}^{-1} \text{cm}^{-2} \text{ster}^{-1}$. (b) We show the fraction of the total opacity provided by electron scattering (solid curve), free-free absorption (dotted curve), and bound-free absorption (dashed curve) evaluated at m_ν^* . (c) The depth of formation (eq. 4) is plotted. (d) The frequency dependent y -parameter (eq. 5) is plotted.

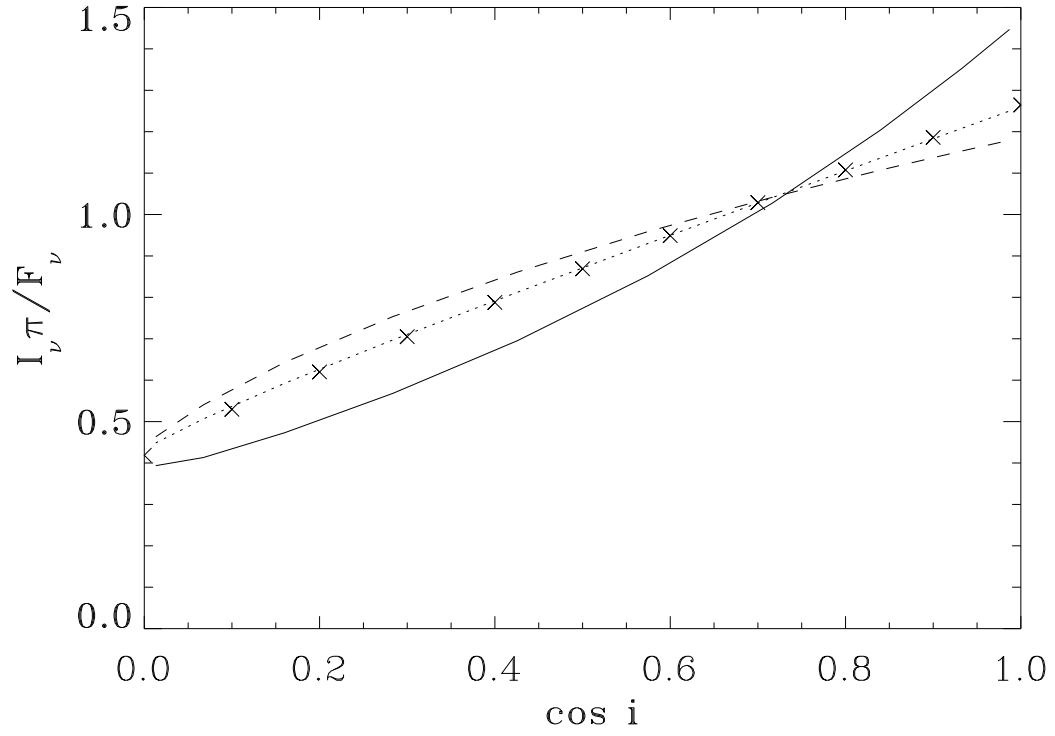


FIG. 2.— Normalized specific intensity of the emission at $r = 12.6$ in an $l = 0.1$, $\alpha = 0.1$, and $a = 0$ disk model. The curves are normalized by a factor of F_ν/π so that isotropic emission would have an ordinate of unity. The curves are plotted for photon energies of 0.21, (dashed) 2.2, (dotted), and 8.4 keV (solid). For comparison we plot the limb darkening law (x's) for a semi-infinite Thomson scattering atmosphere assuming a Rayleigh phase function (Chandrasekhar 1960).

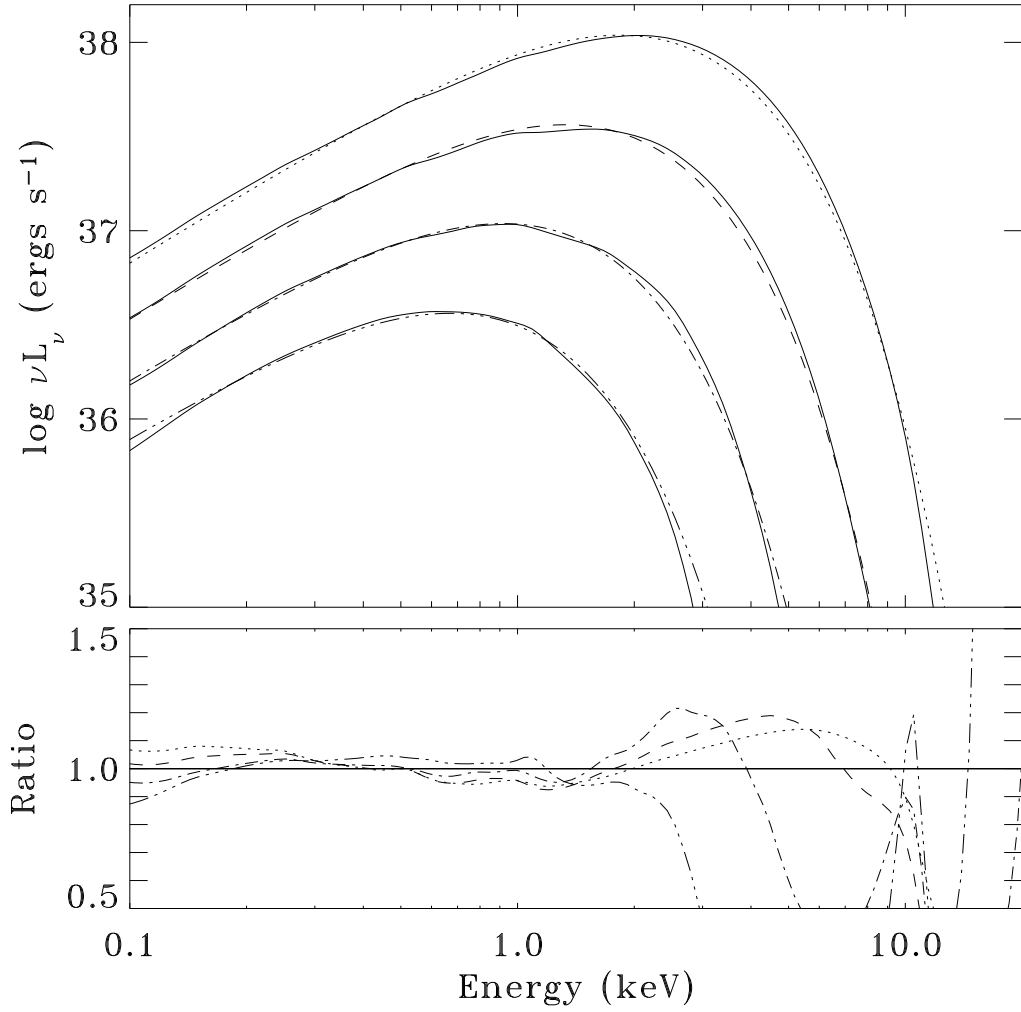


FIG. 3.— Integrated disk SED's of four values of l (solid) viewed at $i = 70^\circ$ by an observer at infinity. At each l , we also plot the best-fit, fully-relativistic disk model spectra in which the local flux is assumed to be an isotropic diluted blackbody. Each model has $\alpha = 0.1$ and $a = 0$ and from lower left to upper right the curves correspond to $l = 0.01, 0.03, 0.1, \text{ and } 0.3$. with best fit $f_{\text{col}} = 1.4$ (triple dot-dashed), 1.46 (dot dashed), 1.56 (dashed), and 1.64 (dotted) respectively. The diluted blackbody spectra are plotted at 81% of their intrinsic luminosity to account for limb darkening in the non-LTE atmosphere models. The lower panel shows the ratio of the non-LTE model spectra to the diluted blackbody spectra.

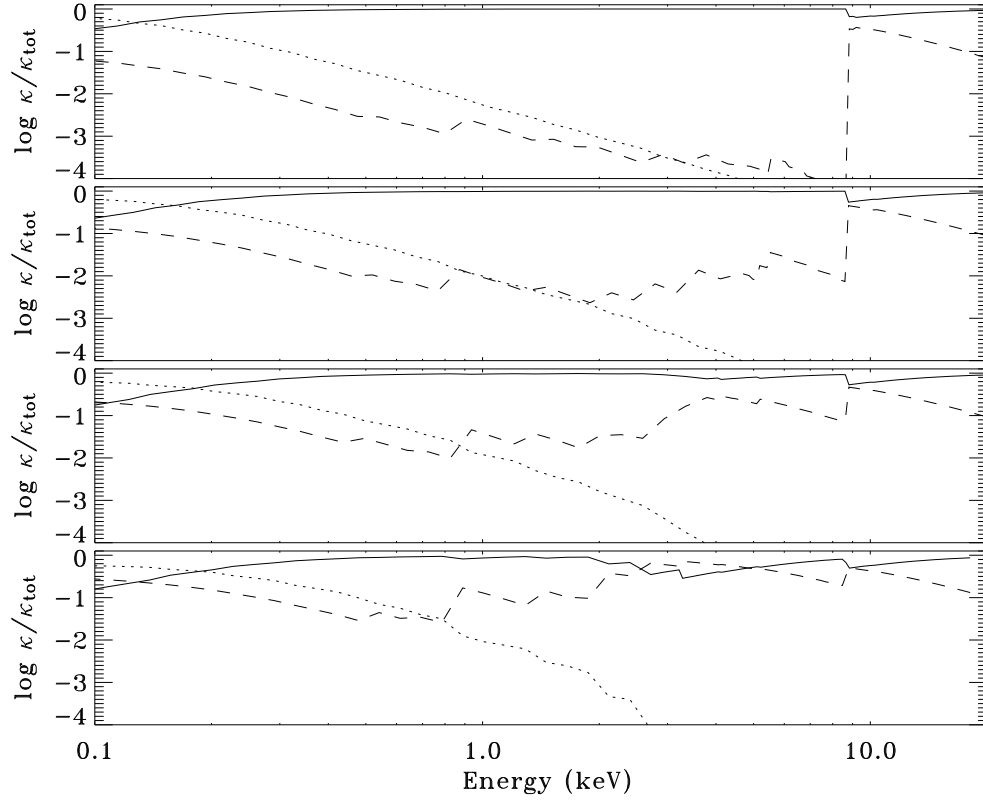


FIG. 4.— Fraction of the total opacity provided by electron scattering (solid), free-free absorption (dotted), and bound-free absorption (dashed) evaluated at m_ν^* and $r = 12.6$ in an $\alpha = 0.1$ and $a = 0$ disk. From top to bottom, the panels correspond to $l=0.3, 0.1, 0.03,$ and 0.01 .

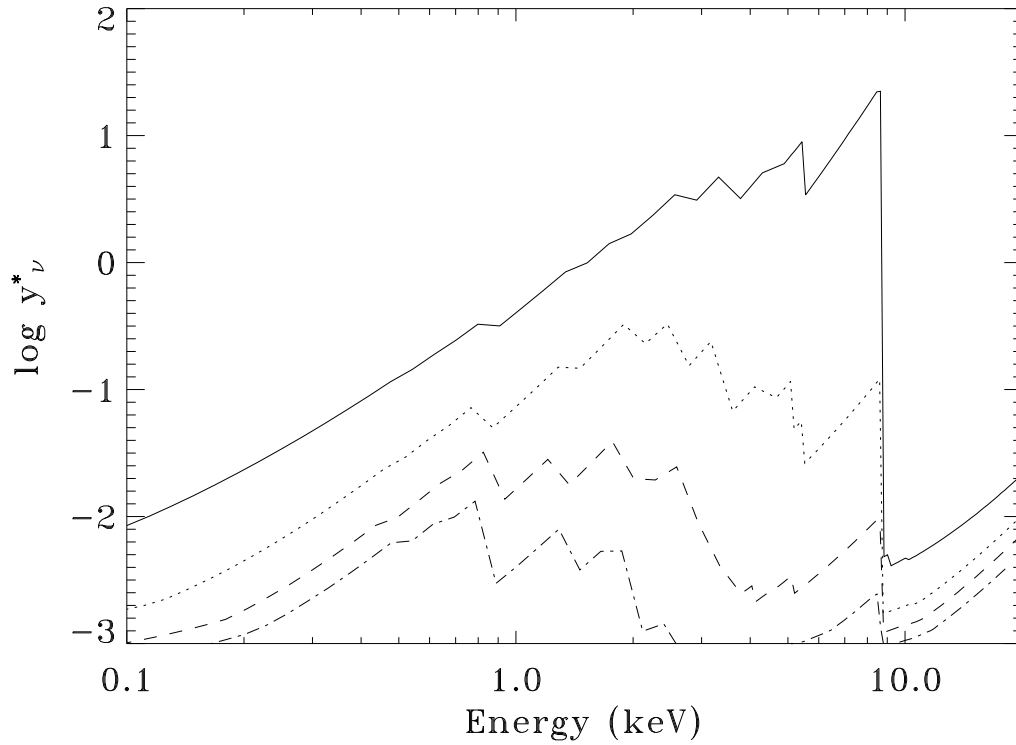


FIG. 5.— Frequency dependent y -parameter, y_ν^* , for models with four different values of l evaluated in the local frame of the disk at $r=12.6$. The curves correspond to $l=0.3$ (solid), 0.1 (dotted), 0.03 (dashed), and 0.01 (dot-dashed).

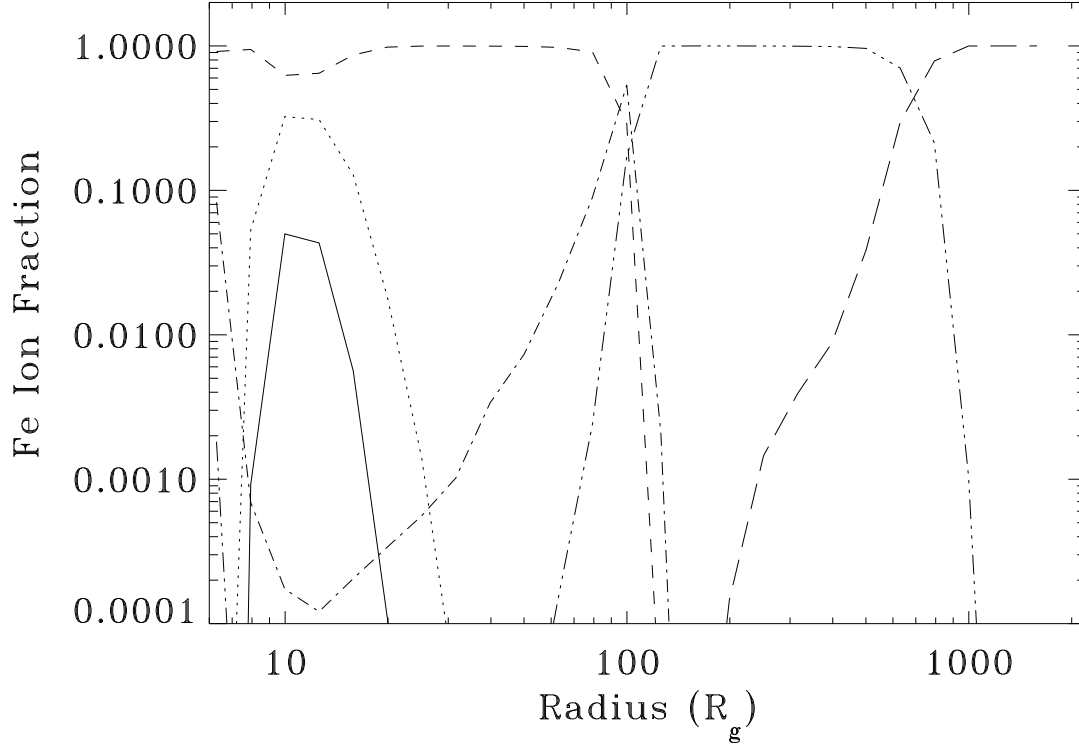


FIG. 6.— Ion fraction of iron at the Thompson photosphere as a function of radius for an $l = 0.3$ and $\alpha = 0.1$ disk accreting onto a Schwarzschild black hole. The curves correspond to Fe XXVII (solid), Fe XXVI (dotted), Fe XXV (short dashed), Fe XXIV (dot-dashed), Fe XXIII (triple dot-dashed), and Fe I - Fe XVI (long dashed).

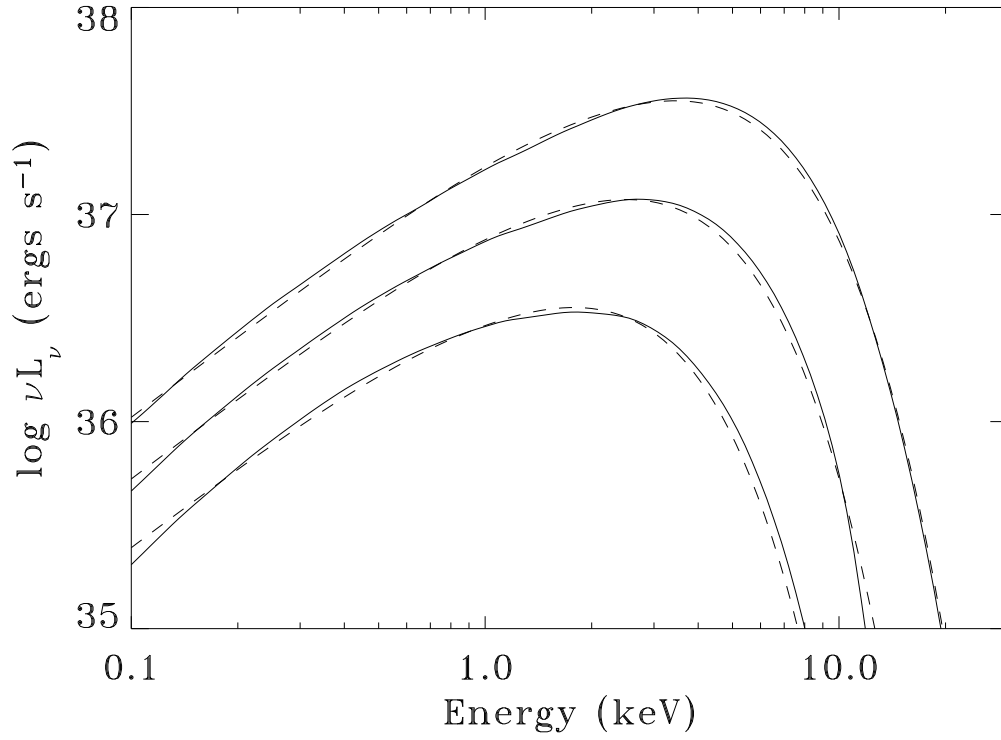


FIG. 7.— Integrated disk SED's for three values of l (solid) observed from an $i = 70^\circ$ by an observer at infinity. At each l , we also plot the best-fit, fully relativistic disk models in which the local flux is assumed to be an isotropic diluted blackbody (dashed). Each model has $\alpha = 0.1$ and $a = 0.998$ and from lower left to upper right the curves correspond to $l = 0.01, 0.03,$ and 0.1 with best fit $f_{\text{col}} = 1.47, 1.53,$ and 1.6 respectively. The diluted blackbody spectra are plotted at 95% of their intrinsic luminosity to account for limb darkening in the non-LTE atmosphere models.

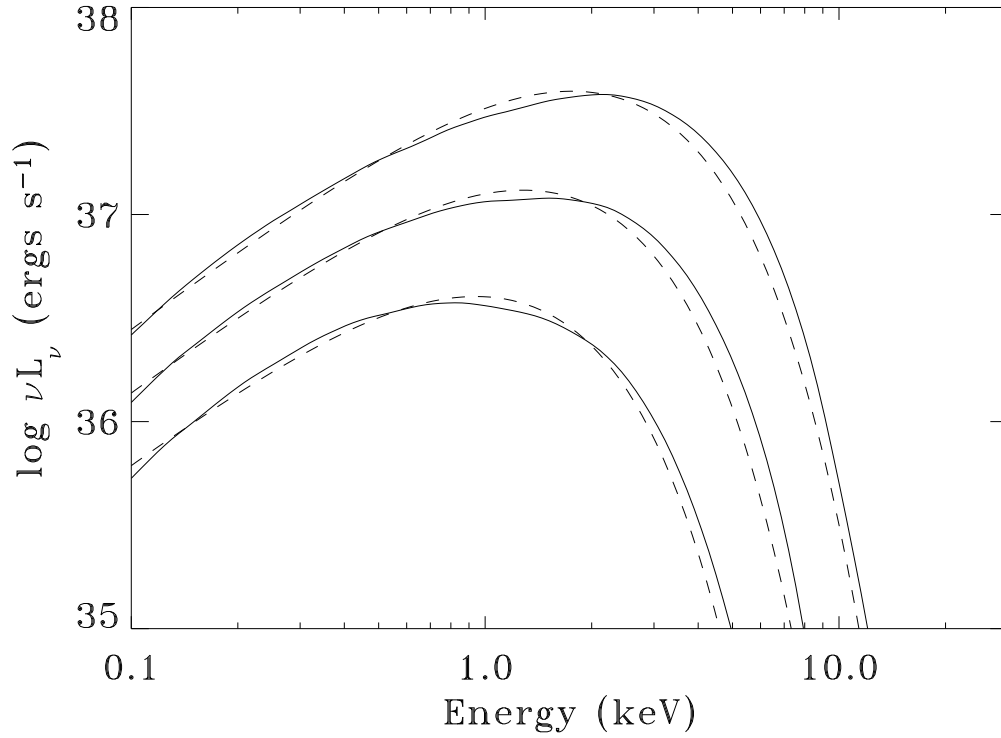


FIG. 8.— Integrated disk SED's for three values of l (solid) observed from an $i = 45^\circ$ by an observer at infinity. At each l , we also plot the best-fit, fully relativistic disk models in which the local flux is assumed to be an isotropic diluted blackbody (dashed). Each model has $\alpha = 0.1$ and $a = 0.998$ and from lower left to upper right the curves correspond to $l = 0.01, 0.03$, and 0.1 with best fit $f_{\text{col}} = 1.4, 1.41$, and 1.47 respectively. The diluted blackbody spectra are plotted at 114% ($l = 0.01$) and 112% ($l = 0.03$ and 0.1) of their intrinsic luminosity to account for limb darkening in the non-LTE atmosphere models.

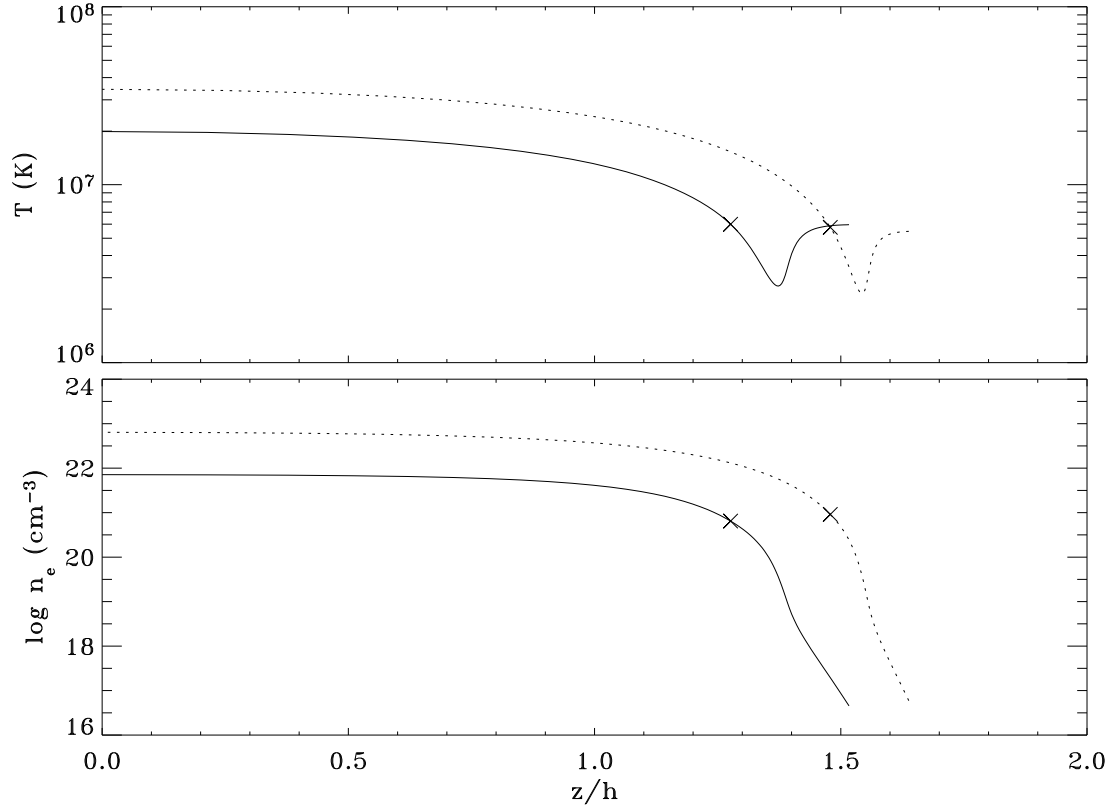


FIG. 9.— Temperature (top) and electron number density (bottom) as a function of height above the midplane. The atmospheres are located at $r = 12.6$ in a disk accreting on to a Schwarzschild black hole with $l = 0.1$ and $\alpha = 0.1$ (solid) or 0.01 (dotted). The x's mark the position of τ_ν^* evaluated for photon frequencies near the peak ($\nu_{\text{peak}} \approx 5 \times 10^{17} \text{ Hz}^{-1}$) of the SED. The scale height, h , is evaluated using a radiation pressure dominated one-zone calculation (HH98 eq. 53).

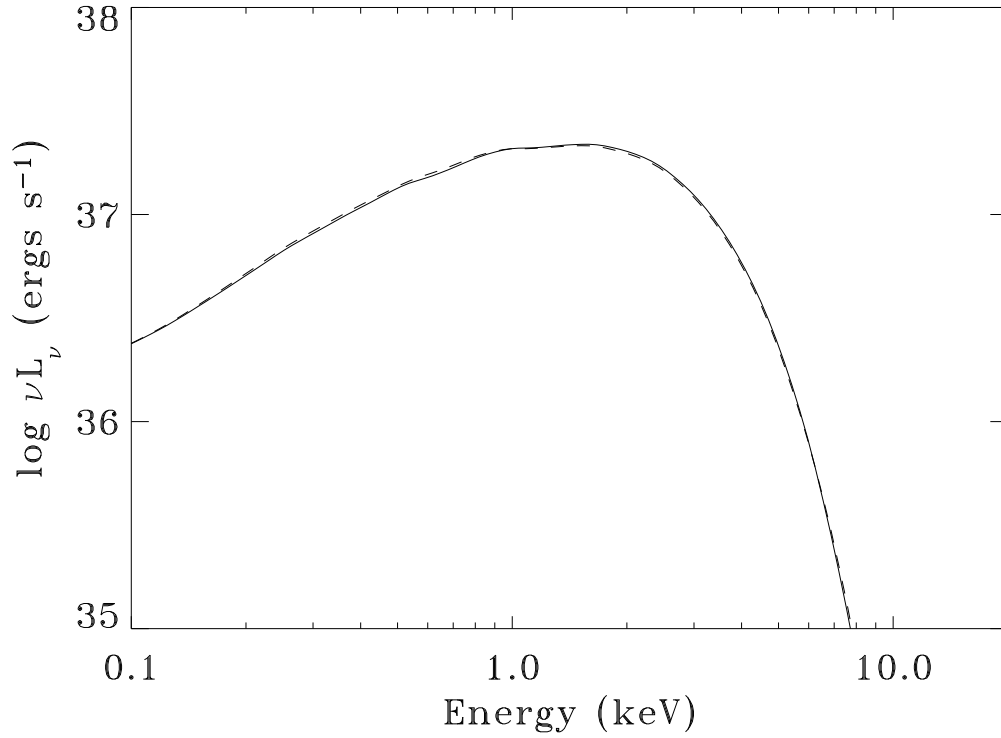


FIG. 10.— Integrated SED's observed at $i = 70^\circ$ by an observer at infinity for disk with $l = 0.1$ and $a = 0$. The curves with $\alpha = 0.1$ (solid) and 0.01 (dashed) are nearly indistinguishable.

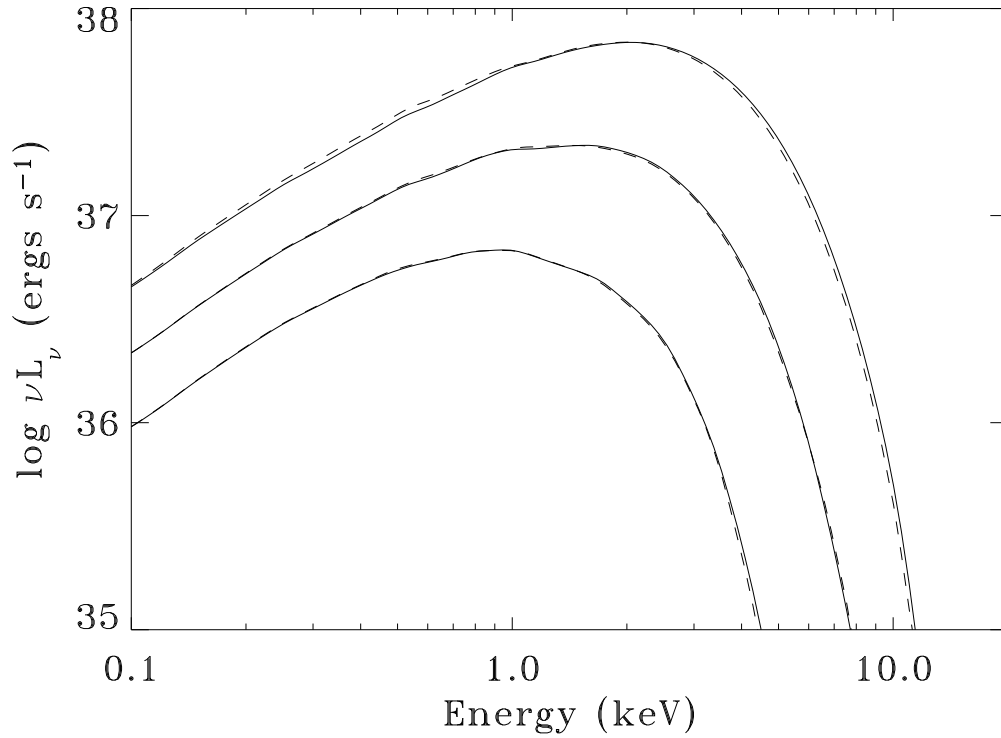


FIG. 11.— Integrated disk SED's for three values of l observed at $i = 70^\circ$ by an observer at infinity. Each model has $\alpha = 0.1$ and $a = 0$ and from lower left to upper right the curves correspond to $l = 0.03, 0.1,$ and 0.3 . The α -disks (solid) are equivalent to the curves plotted in Figure 3. The β -disks (dashed) show little deviation from the α -disks.

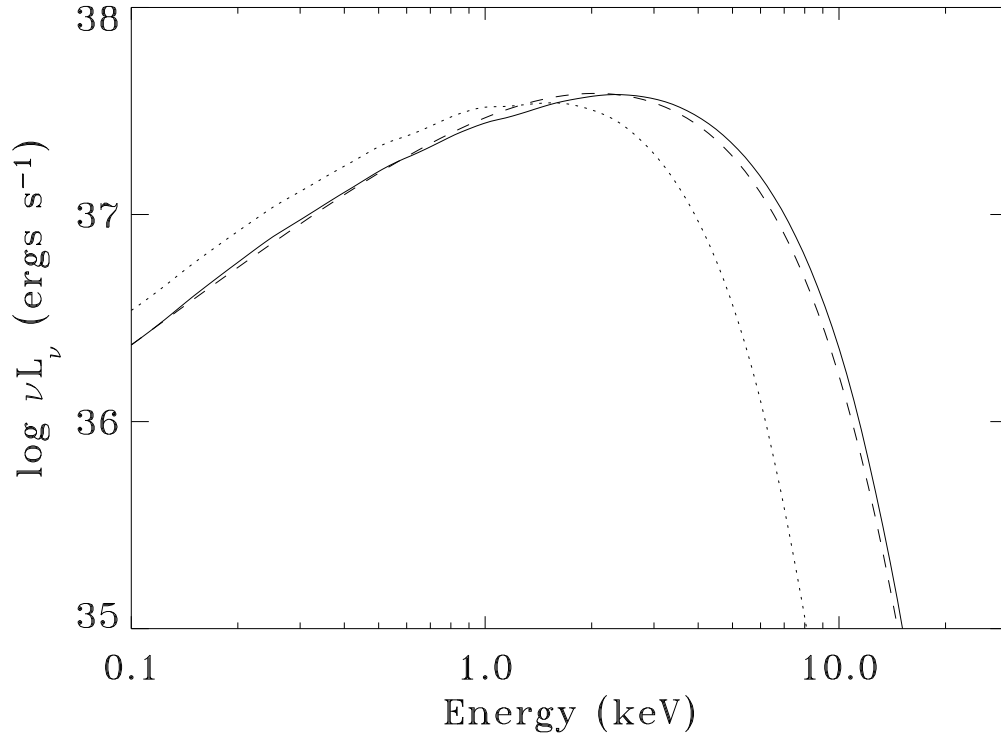


FIG. 12.— SED (solid) from a torqued disk with $l = 0.1$, $a = 0$, $\alpha = 0.1$, and $\Delta\eta = 0.05$ viewed at $i = 70^\circ$ by an observer at infinity. We also plot the best-fit, fully relativistic disk models in which the local flux is assumed to be an isotropic diluted blackbody with $f_{\text{col}} = 1.61$ (dashed). The diluted blackbody spectra are folded through the same transfer function and viewed at the same inclination as the solid curve. The SED of the torqued disk is considerably harder than the SED of of disk without a torque (dotted).

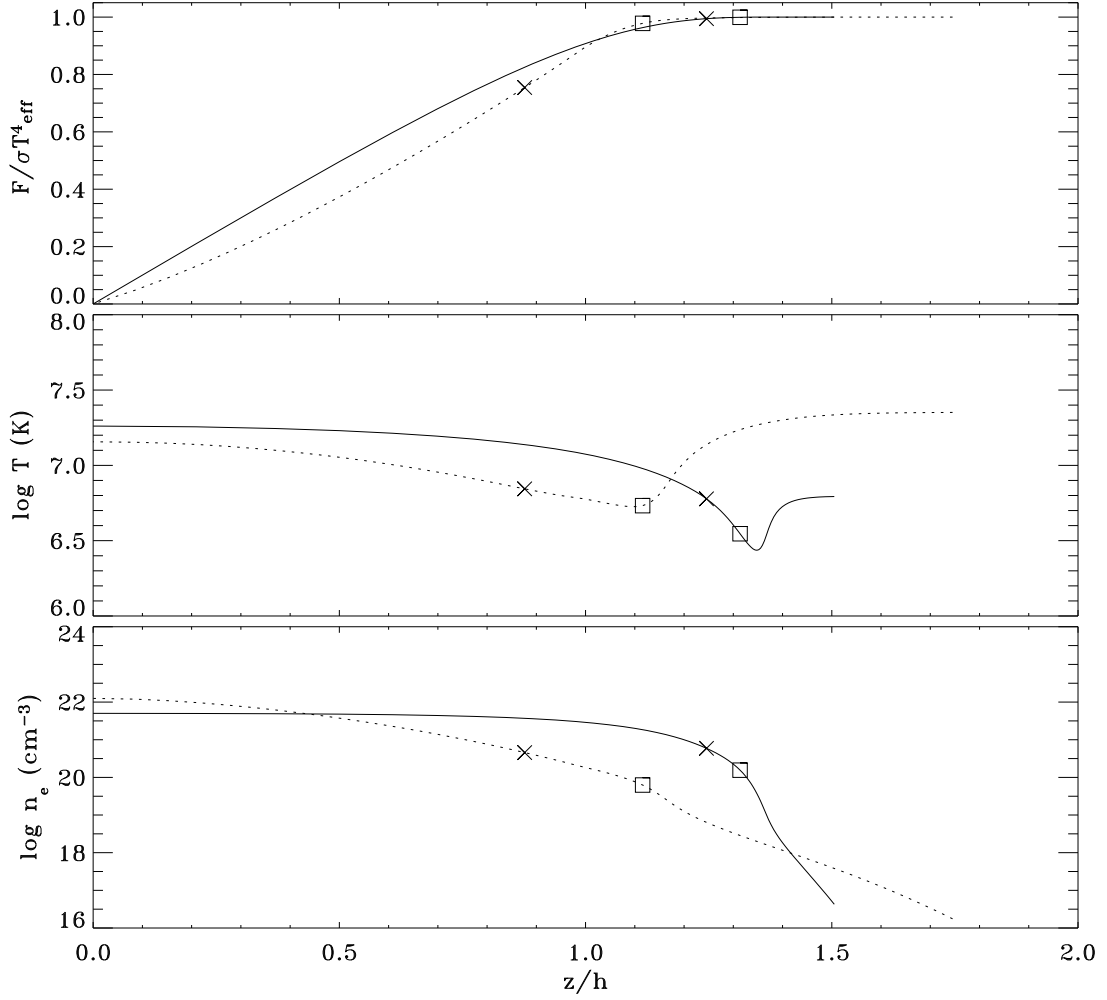


FIG. 13.— Radiative flux (top), temperature (middle) and electron number density (bottom) as a function of height above the midplane. The atmospheres have Q , m_0 , and T_{eff} appropriate for $r = 12.6$ in a disk accreting on to a Schwarzschild black hole with $\alpha = 0.1$. We compare the standard model ($\zeta_0 = \zeta_1 = 0$; solid curve) to a model with a modified dissipation profile ($\zeta_0 = -0.9$, $\zeta_1 = 0$, $f_d = 0.004$; dotted curve). The squares mark the position of the Thomson photosphere and the x's mark τ_d^* evaluated for photon frequencies near the peak ($\nu_{\text{peak}} \approx 5 \times 10^{17} \text{ Hz}^{-1}$) of the SED. The scale height, h , is evaluated using a radiation pressure dominated one-zone calculation (HH98 eq. 53).

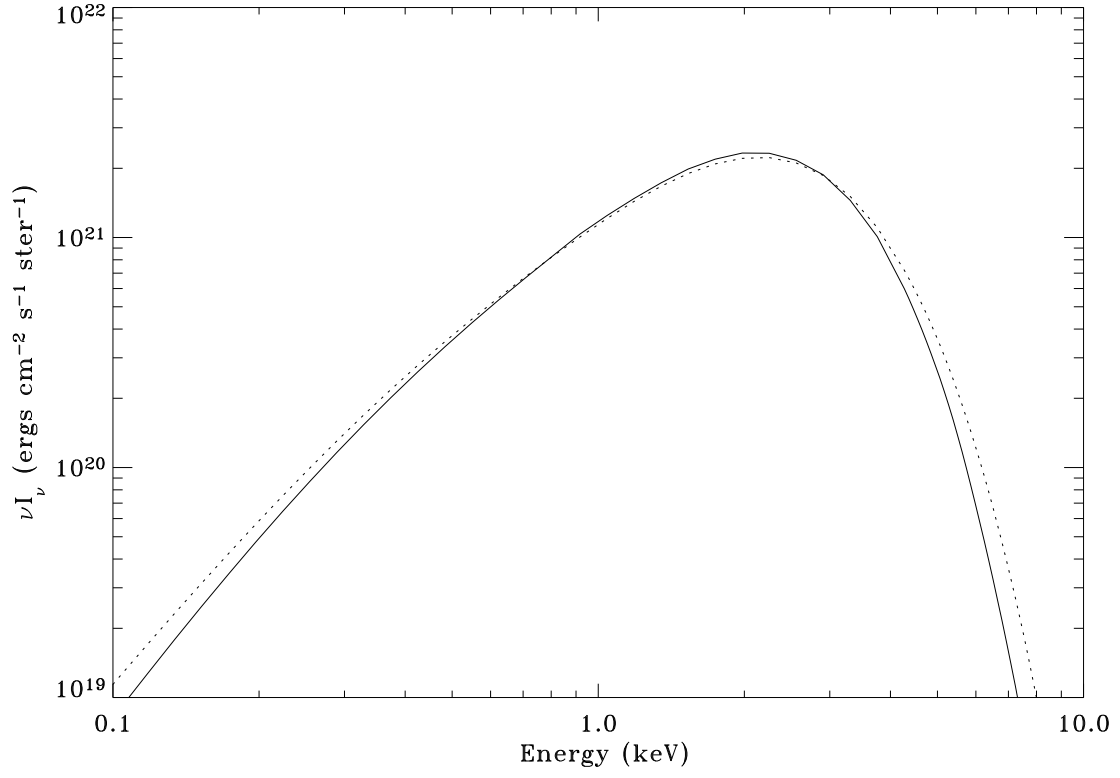


FIG. 14.— Specific intensity viewed at $i = 55^\circ$ in the local frame for the annuli shown in Figure 13. The models parameters are $\zeta_0 = \zeta_1 = 0$ (solid curve), $\zeta_0 = 0.9$, $\zeta_1 = 0$, and $f_d = 0.004$ (dotted curve).

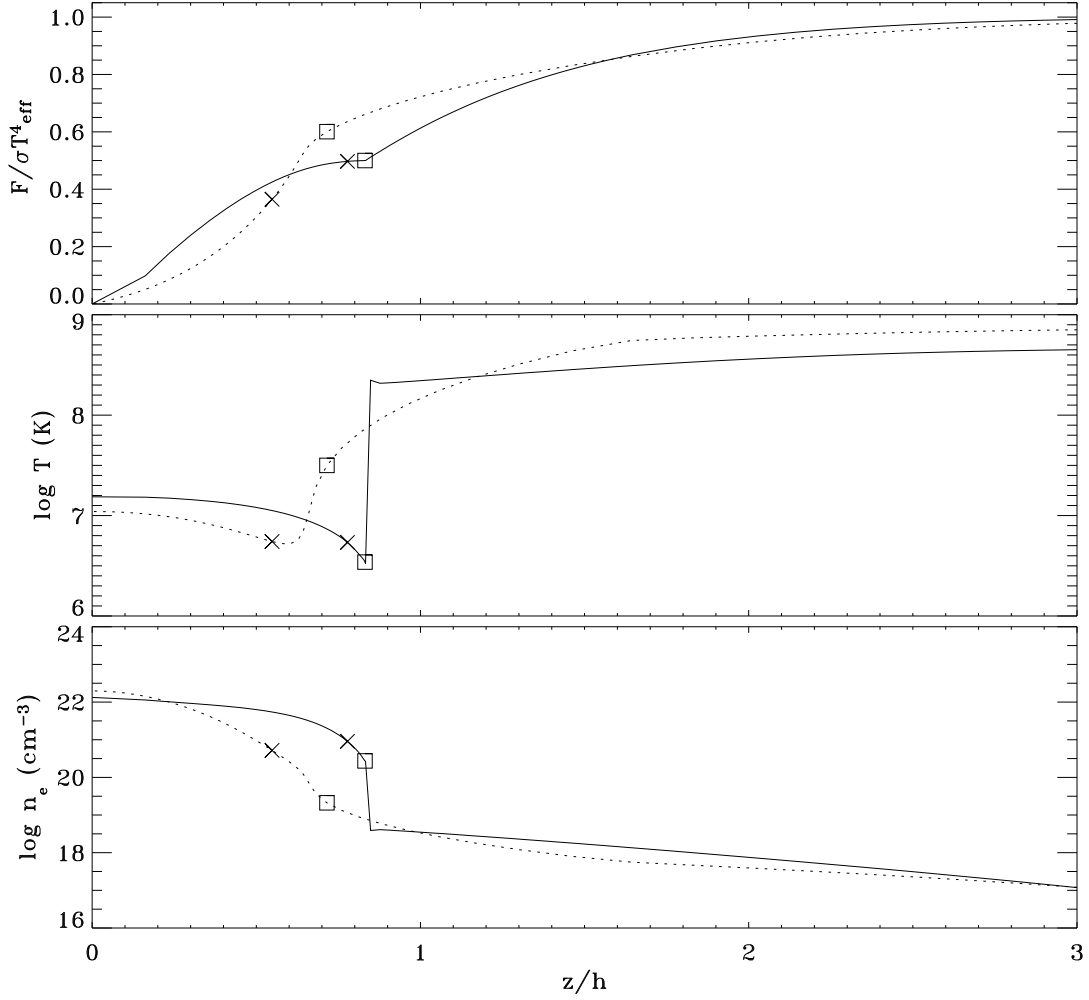


FIG. 15.— Radiative flux (top), temperature (middle) and electron number density (bottom) as a function of height above the midplane. The atmospheres have Q , m_0 , and T_{eff} appropriate for $r = 12.6$ in a disk accreting on to a Schwarzschild black hole with $\alpha = 0.1$. The first model (solid curve) is similar to a standard model annulus ($\zeta_0 = \zeta_1 = 0$) except that dF/dm is not continuous and 50% of the flux is dissipated above the Thompson photosphere. The second model (dashed curve) has a continuous dF/dm with $\zeta_0 = -1.1$, $\zeta_1 = 0$, and $f_d = 0.0001$. About 40% of the dissipation occurs above Thompson depth unity. The squares mark the position of the Thompson photosphere and the x's mark τ_ν^* evaluated for photon frequencies near the peak ($\nu_{\text{peak}} \approx 5 \times 10^{17} \text{ Hz}^{-1}$) of the SED. The scale height, h , is evaluated using a radiation pressure dominated one-zone calculation (HH98 eq. 53).

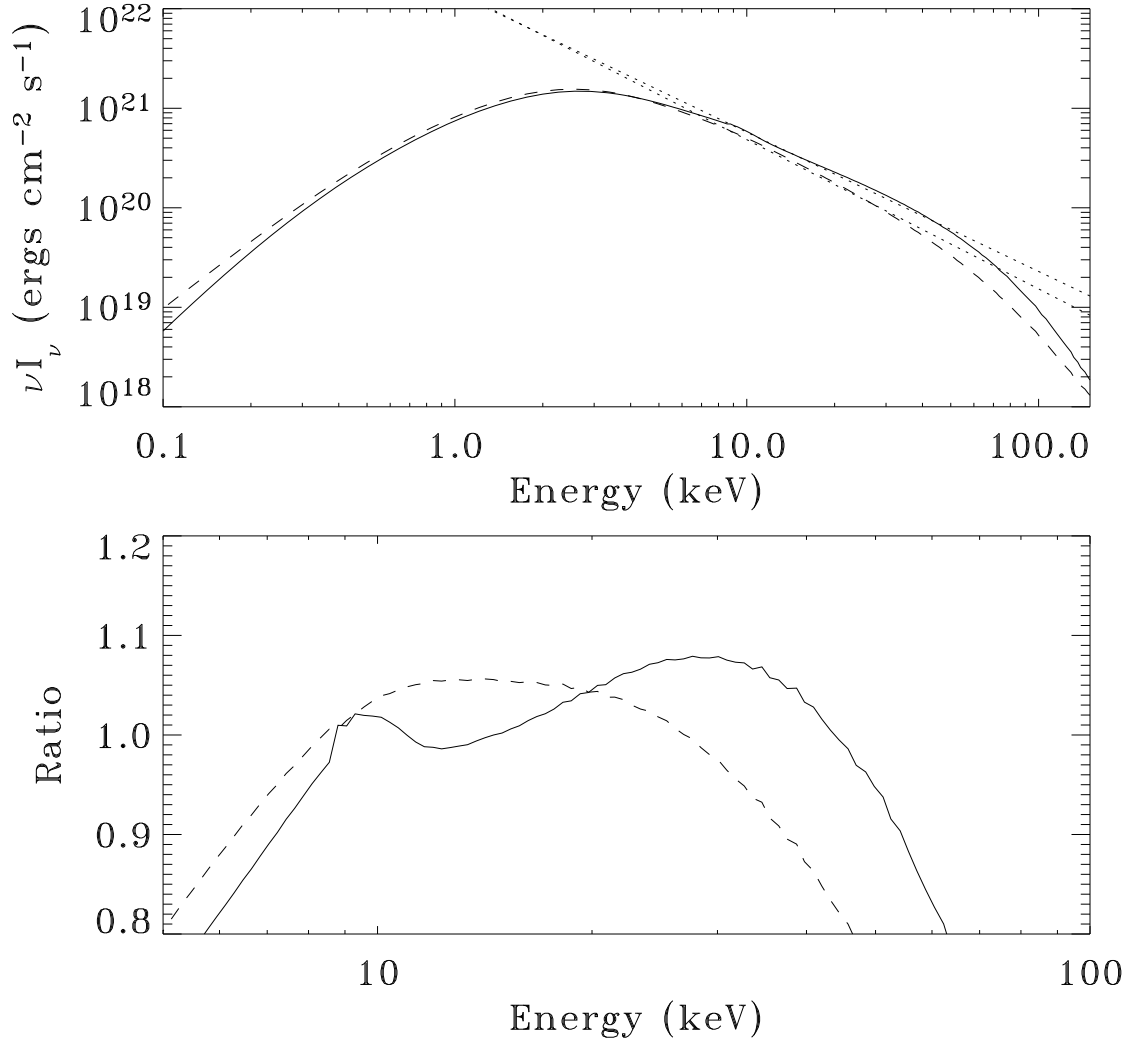


FIG. 16.— Specific intensity viewed at $i = 55^\circ$ in the local frame for the annuli shown in Figure 15. The first model (solid curve) is similar to a standard model annulus ($\zeta_0 = \zeta_1 = 0$) except that dF/dm is not continuous and 50% of the flux is dissipated above the Thomson photosphere. The second model (dashed curve) has a continuous dF/dm with $\zeta_0 = -1.1$, $\zeta_1 = 0$, and $f_d = 0.0001$

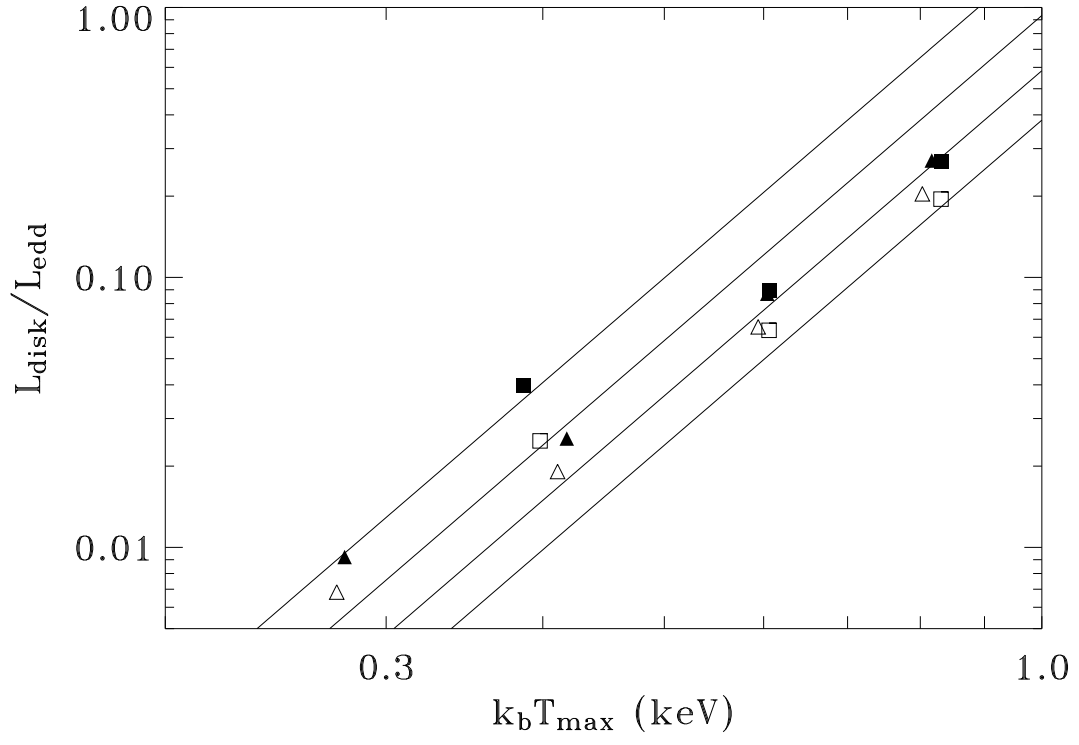


FIG. 17.— Luminosity-temperature relation measured for four Schwarzschild disks viewed at $i = 45^\circ$ (filled symbols) and 70° (open symbols). The solid curves represent the lines of constant $f_{\text{col}} = 1.4, 1.6, 1.8,$ and 2.0 (from top to bottom) from equation 8. The triangles and squares mark the *XMM* EPIC-PN and *RXTE* PCA measurements respectively.

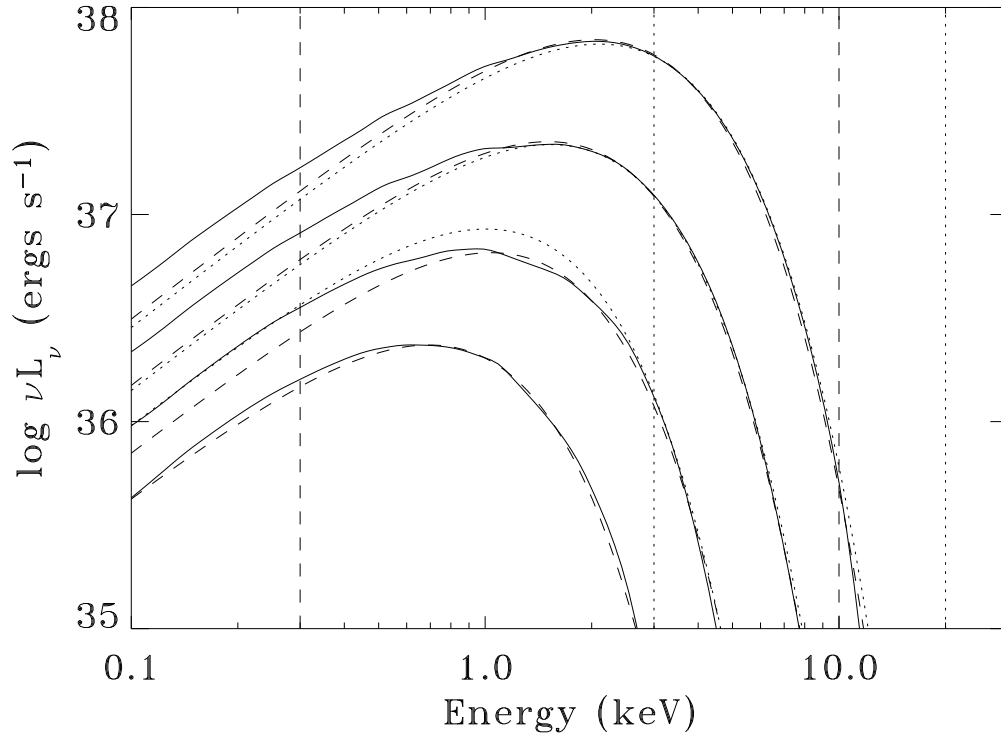


FIG. 18.— Integrated non-LTE disk SED's from Figure 3 (solid curve). At each i , we also plot the best-fit *diskbb* models for the *XMM-Newton* EPIC-pn (dashed) and *RXTE* PCA (dotted) artificial data sets. The vertical solid and dashed lines mark the endpoints of EPIC-pn and PCA energy ranges respectively.